# Inorganic Chemistry

# Heteroleptic Samarium(III) Chalcogenide Complexes: Opportunities for Giant Exchange Coupling in Bridging $\sigma$- and $\pi$-Radical Lanthanide Dichalcogenides

Conrad A. P. Goodwin, Benjamin L. L. Réant, Gianni F. Vettese, Jon G. C. Kragskow, Marcus J. Giansiracusa, Ida M. DiMucci, Kyle M. Lancaster, David P. Mills,* and Stephen Sproules*

Cite This: https://dx.doi.org/10.1021/acs.inorgchem.0c00470

Read Online

ACCESS | Metrics & More | Article Recommendations | SI Supporting Information

**ABSTRACT:** The introduction of $(N_2)^{3-\bullet}$ radicals into multinuclear lanthanide molecular magnets raised hysteresis temperatures by stimulating strong exchange coupling between spin centers. Radical ligands with larger donor atoms could promote more efficient magnetic coupling between lanthanides to provide superior magnetic properties. Here, we show that heavy chalcogens (S, Se, Te) are primed to fulfill these criteria. The moderately reducing Sm(II) complex, $[Sm(N^{\dagger\dagger})_2]$, where $N^{\dagger\dagger}$ is the bulky bis(triisopropylsilyl)-amide ligand, can be oxidized (i) by diphenyldichalcogenides $E_2Ph_2$ (E = S, Se, Te) to form the mononuclear series $[Sm(N^{\dagger\dagger})_2(EPh)]$ (E = S, **1-S**; Se, **1-Se**, Te, **1-Te**); (ii) $S_8$ or $Se_8$ to give dinuclear $[\{Sm(N^{\dagger\dagger})_2\}_2(\mu\text{-}\eta^2:\eta^2\text{-}E_2)]$ (E = S, **2-S$_2$**; Se, **2-Se$_2$**); or (iii) with Te=PEt$_3$ to yield $[\{Sm(N^{\dagger\dagger})_2\}_2(\mu\text{-Te})]$ (**3**). These complexes have been characterized by single crystal X-ray diffraction, multinuclear NMR, FTIR, and electronic spectroscopy; the steric bulk of $N^{\dagger\dagger}$ dictates the formation of mononuclear complexes with chalcogenate ligands and dinuclear species with the chalcogenides. The $L\alpha_1$ fluorescence-detected X-ray absorption spectra at the Sm L$_3$-edge yielded resolved pre-edge and white-line peaks for **1-S** and **2-E$_2$**, which served to calibrate our computational protocol in the successful reproduction of the spectral features. This method was employed to elucidate the ground state electronic structures for proposed oxidized and reduced variants of **2-E$_2$**. Reactivity is ligand-based, forming species with bridging superchalcogenide $(E_2)^{-\bullet}$ and subchalcogenide $(E_2)^{3-\bullet}$ radical ligands. The extraordinarily large exchange couplings provided by these dichalcogenide radicals reveal their suitability as potential successors to the benchmark $(N_2)^{3-\bullet}$ complexes in molecular magnets.
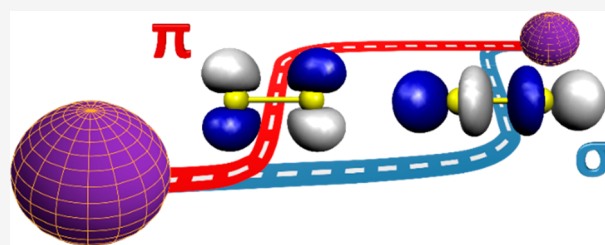
## INTRODUCTION

The concept of Hard and Soft Acids and Bases (HSAB) presents a challenge for synthetic chemists aiming to bind heavy chalcogens to f-elements, as there is a dichotomy between large and diffuse soft Lewis bases and highly electropositive hard f-block ions.[1] For this reason, the chemistry of the f-block with sulfur, selenium, and tellurium has lagged behind that of their more congenial partner oxygen. However, it is precisely this hard/soft mismatch that makes lanthanide (Ln) chalcogenide complexes so appealing as synthetic targets, producing reactive Ln centers that can serve as intermediates in organic transformations[2] or as precursors to materials with highly desirable physicochemical properties.[3] The weak bonding interaction supplied by heavy chalcogens has been successfully exploited for the selective extraction of Ln from actinides (An) in the partitioning of nuclear waste, where bidentate S,S'-dithiophosphinate chelates display exceptional performance.[4,5]

The recent surge in f-element chemistry with heavy chalcogens has not yet been fully exploited in molecular magnetism, where the intrinsically large magnetic anisotropy of Ln makes them enormously popular.[4–7] The few molecular

magnets that incorporate ligands comprising larger main group elements have performance characteristics that eclipse their lighter counterparts, such as a higher thermal barrier to magnetization reversal.[8] A key component in the design of molecular magnets is the exchange interaction between paramagnetic centers,[9] thus the inclusion of heavy chalcogens with their radially extended p-orbitals is advantageous. The exchange interaction in Ln systems was often ignored until the arrival of a series of dilanthanide complexes bearing a highly reduced $(N_2)^{3-\bullet}$ radical ligand that produced record high exchange couplings with exceptional magnetic performance to match,[9–11] promoting a re-evaluation of magnetic exchange mechanisms in molecular magnets and materials for related emergent technologies.[9,12,13]

A

Modifying the infrastructure to replace the highly reactive dinitrogen bridge with more tractable redox-active ligands has brought greater chemical versatility to these systems but has simultaneously diminished the exchange interaction as more atoms are added to the coupling pathway.[14] Therefore, we propose dichalcogenides as potential successors to the dinitrogen ligand as they provide a single atom link and diffuse p orbitals that offer a more efficient coupling route.[15] The most compelling attribute of dichalcogenides is their facile redox chemistry: the archetypal dichalcogenide $(E_2)^{2-}$ is readily reduced to the subchalcogenide oxidation level, $(E_2)^{3-\bullet}$, which is analogous to $(N_2)^{3-\bullet}$ but with a $\sigma^*$ magnetic orbital (Figure 1). Dichalcogenides can also be oxidized to
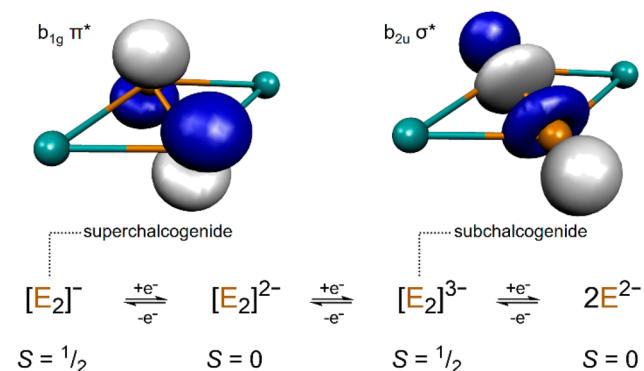


**Figure 1.** One-electron redox processes in the bridging dichalcogenide $(E_2)$ ligand and accompanying spin state for each species. The singly occupied molecular orbitals (SOMO) are shown for paramagnetic super- and subchalcogenides with $D_{2h}$ symmetry.

superchalcogenides, $(E_2)^{-\bullet}$, which are $\pi$-radical ligands that are isoelectronic with $(N_2)^{3-\bullet}$. Both of these radical species are stabilized through coordination to metal ions, as highlighted in a series of rigorous electronic structure studies recently reported by Berry et al.[16−19]

Synthetic access to Ln heavy chalcogen species typically occurs by cleaving E−E bonds in chalcogen-containing compounds, which can be achieved by a Ln(II) reductant.[20−23] Here, a series of low-coordinate Sm−E complexes are produced from the oxidation of $[Sm(N^{\dagger\dagger})_2]$ $(N^{\dagger\dagger} = \{N(Si^iPr_3)_2\})^{[16-19,24,25]}$ with (i) diphenyldichalcogenides $E_2Ph_2$ (E = S, **1-S**; Se, **1-Se**, Te, **1-Te**), (ii) $S_8$ or $Se_8$ to give $[\{Sm(N^{\dagger\dagger})_2\}_2(\mu-\eta^2:\eta^2-E_2)]$ (E = S, **2-S$_2$**; Se, **2-Se$_2$**), and (iii) Te=PEt$_3$ to yield $[\{Sm(N^{\dagger\dagger})_2\}_2(\mu-Te)]$ (**3**). Their molecular structures are confirmed by single-crystal X-ray diffraction, and electronic structures elucidated by a combination of spectroscopic and computational techniques. Exercising the methodology developed for the analogous halide series,[26] we employ the high resolution provided by fluorescence-detected X-ray absorption spectroscopy (XAS) to experimentally calibrate our density functional theoretical (DFT) method by canvassing a range of calculation parameters. The protocol that gave the best reproduction of the Sm L$_3$-edge by time-dependent (TD) DFT calculations was then applied to an examination of the one-electron oxidized and reduced variants of **2-E$_2$** (E = S, Se), which contain $(E_2)^{-\bullet}$ and $(E_2)^{3-\bullet}$ radical ligands, respectively. The analysis reveals the contrast between $\sigma$ and $\pi$ bridging radical ligands and shows both types afforded exchange couplings either equivalent to or greater than those seen in the $(N_2)^{3-\bullet}$ benchmarks. We also elaborate on the pivotal

importance of the coligand in the design of new radical-bridged complexes with f elements.

## RESULTS AND DISCUSSION

**Synthesis.** The near-linear Sm(II) complex $[Sm(N^{\dagger\dagger})_2]$ was treated with a variety of oxidants in efforts to form homologous terminal Sm−EPh (E = S, Se, Te) and bridged $Sm_2E_n$ (E = S, Se, Te; $n = 1$ or 2) species. Dialkyl- and diaryl-dichalcogenides are commercially available sources of ER$^\bullet$ as the E−E bond can be homolytically cleaved by two single electron transfer (SET) events, i.e., two Sm(II) ions can be oxidized to each gain a coordinated ER$^-$ unit. This methodology was previously employed to synthesize monomeric $[Sm(Cp^*)_2(EPh)(thf)]$ (E = S, Se, Te) and dimeric $[Sm(Cp^*)_2(\mu\text{-}EPh)]_2$ (E = S, Se, Te) complexes from either $[Sm(Cp^*)_2]$ or $[Sm(Cp^*)_2(thf)_2]$.[21] There are numerous examples of analogous reactions across the f block,[20,23,27,28] and these polar M−ER groups (M = Ln or An) are amenable to further derivatization.[29] We have previously shown that although the ligand framework in $[Sm(N^{\dagger\dagger})_2]$ is sterically demanding, the two bis(triisopropylsilyl)amide ligands are flexible enough to bend toward each other to accommodate further moieties at the Sm center, thus we envisaged that this redox strategy would afford a series of structurally similar complexes.[25,26,30] Gratifyingly, the separate reactions of $[Sm(N^{\dagger\dagger})_2]$ with half an equivalent of $E_2Ph_2$ in toluene gave the heteroleptic Sm(III) complexes $[Sm(N^{\dagger\dagger})_2(EPh)]$ (E = S, **1-S**; Se, **1-Se**; Te, **1-Te**; Scheme 1) in moderate to excellent
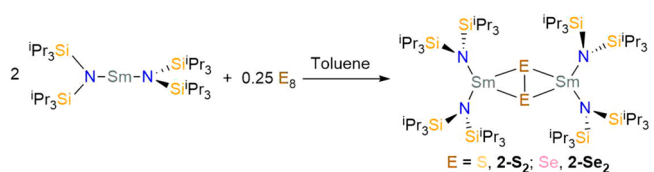
**Scheme 1. Synthesis of $[Sm(N^{\dagger\dagger})_2(EPh)]$ (E = S, Se, Te)**
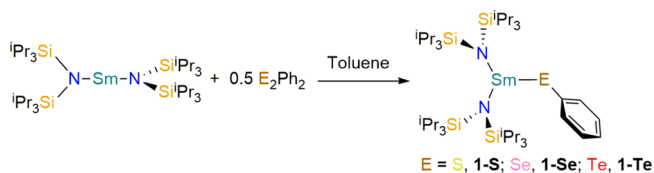


yields (52−93%). Previously, Ln−EPh moieties have been investigated toward reductive elimination of $E_2Ph_2$ in order to access Ln redox chemistry while avoiding the challenging synthesis of divalent precursors.[31]

The syntheses of mono- and polychalcogenido-bridged Sm(III) bis(triisopropylsilyl)amide complexes presented unexpected challenges. Using elemental sulfur in redox processes with f-block complexes is well-documented,[32−34] and the reaction of $[Sm(N^{\dagger\dagger})_2]$ with $^1/_8$ of an equivalent of sulfur gave $[\{Sm(N^{\dagger\dagger})_2\}_2(\mu-\eta^2:\eta^2-S_2)]$ (**2-S$_2$**) in low yield (Scheme 2). The intended product based on stoichiometry was the monosulfido complex, thus the yield was not optimized. Attempts to furnish other $S_n$ polyanions such as $S_3^{2-}$ [33,35] or $S^{2-}$ [32,33,36] by altering the stoichiometry only gave $S_8$, $[Sm(N^{\dagger\dagger})_2]$, and **2-S$_2$**. The homologous diselenido-bridged

**Scheme 2. Synthesis of $[\{Sm(N^{\dagger\dagger})_2\}_2(\mu-\eta^2:\eta^2-E_2)]$ (E = S, Se)**

Sm(III) complex $[\{Sm(N^{\dagger\dagger})_2\}_2(\mu\text{-}\eta^2{:}\eta^2\text{-Se}_2)]$ (**2-Se$_2$**) was also synthesized by treating $[Sm(N^{\dagger\dagger})_2]$ with $^1/_8$ of an equivalent of Se$_8$ in similar yield to **2-S$_2$** (Scheme 2).

Reactions of $[Sm(N^{\dagger\dagger})_2]$ with P(V) chalcogen atom transfer reagents E=PR$_3$ (R = Ph, E = S, Se; R = Et, E = S, Se, Te)[37] were uniformly sluggish, despite heating at 100 °C for several days (see Supporting Information). However, in one instance, prolonged heating of $[Sm(N^{\dagger\dagger})_2]$ and Te=PEt$_3$ gave single crystals of the monochalcogenido-bridged $[\{Sm(N^{\dagger\dagger})_2\}_2(\mu\text{-}Te)]$ (**3**) after standing for 2 weeks (Scheme 3).

**Scheme 3. Synthesis of $[\{Sm(N^{\dagger\dagger})_2\}_2(\mu\text{-Te})]$**
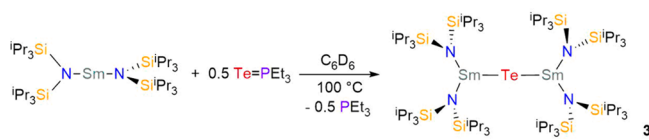


**NMR Spectroscopy.** The $^1$H NMR spectra of **1-E** each show two broad signals corresponding to the N$^{\dagger\dagger}$ ligand and were assigned based on integration. The methine peak positions shift downfield as the chalcogen electronegativity decreases ($\delta_H$ = **1-S**, −8.61; **1-Se**, −8.47; **1-Te**, −8.30 ppm), whereas the methyl peak positions are invariant ($\delta_H$ = **1-S**, 0.24; **1-Se**, 0.22; **1-Te**, 0.21 ppm). The proton resonances for the −EPh group in **1-E** were not noticeably broadened by the paramagnetic Sm(III) center, with three peaks discernible for **1-S** and **1-Te** and the *meta*-protons in **1-Se** masked by the solvent residual. The solution phase dynamics in **1-S** were examined by monitoring the temperature dependence of the SPh proton resonances (Figure S40). The $^{13}$C{$^1$H} NMR spectra show two sharp peaks for the N$^{\dagger\dagger}$ ligand with the methine peak shifted upfield in the order of decreasing chalcogen electronegativity ($\delta_C$ = **1-S**, 15.66; **1-Se**, 15.55; **1-Te**, 15.39 ppm). The methyl peak was again invariant ($\delta_C$ = **1-S**, 19.82; **1-Se**, 19.77; **1-Te**, 19.83 ppm). The nonquaternary EPh resonances for **1-E** were observed ($\delta_C$ = **1-S**, 123.77, 128.68, 130.57; **1-Se**, 123.77, 130.22, 134.97; **1-Te**, 124.60, 129.91, 140.76 ppm), with the peaks assigned to the *ortho*-C shifted upfield with decreasing chalcogen electronegativity. This trend has been noted in the related Sm(III) complexes $[Sm(Cp^*)_2(EPh)(thf)]$.[21] The $^1$H NMR spectra of **2-E$_2$** contained multiple broad signals and could only be tentatively assigned due to their integrals being affected by the presence of diamagnetic HN$^{\dagger\dagger}$.

**Magnetometry.** Room temperature solution phase magnetic moments determined for **1-E** and **2-E$_2$** using the Evans method[38] are consistent with other Sm(III)-N$^{\dagger\dagger}$ species (Table 1).[24−26,30] The solution moments for **1-E** are higher than the room temperature $\chi_M T$ products that range 0.14−0.19 cm$^3$ K mol$^{-1}$ from magnetometric measurements on powder samples, though both are noticeably larger than the free-ion value for a $^6H_{5/2}$ multiplet at 0.09 cm$^3$ K mol$^{-1}$.[39] This is characteristic of Sm(III), where the observed moment is dominated by

temperature independent paramagnetism from second-order mixing with low-lying excited states.[39,40] On cooling, $\chi_M T$ steadily decreases to 0.03 cm$^3$ K mol$^{-1}$ at 2 K (Figures S45, S47, and S49). Magnetization traces recorded at 2 and 4 K are distinct, though they fail to saturate as a function of the applied field up to 7 T. As was the case for the monometallic compounds, the magnetic moments for **2-E$_2$** are higher than would be expected for two isolated Sm(III) centers (Table 1). The discrepancy between the values for **2-S$_2$** and **2-Se$_2$** could be due to differences in the additive coupling of the two magnetic moments facilitated by the dichalcogenide bridge, as well as the significantly larger different spin−orbit contribution from selenium compared with sulfur.

**Structural Characterization.** The crystal structures of **1-E** have been determined by single crystal X-ray crystallography at 150 K. The molecular structures are presented in Figure 2; selected bond distances and angles are summarized in Table 2. Complexes **1-E** are all monomeric in the solid state, with approximate trigonal planar geometry about the Sm(III) ion (range Sm···N$_2$E plane distance 0.065−0.082 Å). The Sm(III) centers are coordinated by the corresponding chalcogenide and two monodentate N$^{\dagger\dagger}$ ligands. The average Sm−N distance shortens as the Sm−E distance increases, which is governed by the size of the chalcogenide (S$^{2-}$, 1.84 Å; Se$^{2-}$, 1.98 Å; Te$^{2-}$, 2.21 Å). The incremental lengthening of the Sm−E bond on descent of group 16 is in excellent agreement with the related monomeric complexes $[Sm(Cp^*)_2(EPh)$-$(thf)]$,[21] although the analogous distances in **1-E** are slightly shorter on account of their coordination number. The N−Sm−N angle is shifted significantly from 120° in all three complexes, though the magnitude decreases on descending the group (**1-S**, 138.33(7)°; **1-Se**, 132.7(2)°; **1-Te**, 128.6(1)°). The Sm−E−C angles also decrease from S to Te because of attenuated s-p hybridization in the frontier orbitals of the heavier chalcogens pushing the angle closer to 90°.[41] The coordination spheres of **1-E** are completed by several short C−H···Sm contacts, with the shortest Sm−C distances usually ~3.1 Å. These interactions are ubiquitous in f-element complexes of these bulky bis(silyl)amide ligands and have been discussed in detail previously.[26,30,42−44]

Complexes **2-S$_2$** and **2-Se$_2$** both crystallize in the $P2_1/n$ space group with one molecule in the asymmetric unit. Both complexes feature two $\{Sm(N^{\dagger\dagger})_2\}$ fragments linked by a $\mu$-$\eta^2{:}\eta^2$-E$_2^{2-}$ ligand (Figure 3), with E−E distances typical for S$_2^{2-}$ of 2.1075(10) Å and Se$_2^{2-}$ of 2.3662(7) Å consistent with their dianionic formulation.[18,19] For example, in $[\{Y$-$(N'')_2(thf)\}_2(\mu\text{-}\eta^2{:}\eta^2\text{-E}_2)]$ (N'' = $\{N(SiMe_3)_2\}$; E = S, Se) the S−S distance is 2.118(2) Å and the Se−Se distance is 2.399(5) Å.[33] The monodentate N$^{\dagger\dagger}$ ligands have Sm−N lengths that are typical for Sm(III) bound to this ligand (Table 3).[26,30] The SmN$_2$ units are canted relative to each other, with a dihedral angle ($\theta$) between the mean planes of the terminal SmN$_2$ groups residing at 45.8(1)° and 45.3(1)° for **2-S$_2$** and **2-Se$_2$**, respectively. To the best of our knowledge **2-S$_2$** represents the first structurally characterized example of a Sm$_2$S$_2$ unit despite several examples of Yb$_2$S$_2$ species generated from similar reagents.[23,45,46] The distinguishing features in **2-S$_2$** are the long Sm−S distances, which are ca. 0.1 Å longer than in any related Ln$_2$S$_2$ species.[23,33,34,45−47] A recently reported Nd$_2$S$_2$ complex has the same dimensions as the Sm$_2$S$_2$ core in **2-S$_2$**,[48] despite Nd(III) having a larger ionic radius.[49] The long Sm−S bonds are the result of the steric demands of the N$^{\dagger\dagger}$ ligand, which limits the Sm···Sm distance to 5.273(1) Å. In

**Table 1. Room Temperature $\chi_M T$ Values (cm$^3$ K mol$^{-1}$) Determined by Evans Solution NMR and Solid-State SQUID Magnetometry**

|  | 1-S | 1-Se | 1-Te | 2-S$_2$ | 2-Se$_2$ |
|---|---|---|---|---|---|
| Evans | 0.37 | 0.34 | 0.40 | 0.48 | 0.64 |
| SQUID | 0.18 | 0.14 | 0.19 | 0.35 | 0.46 |
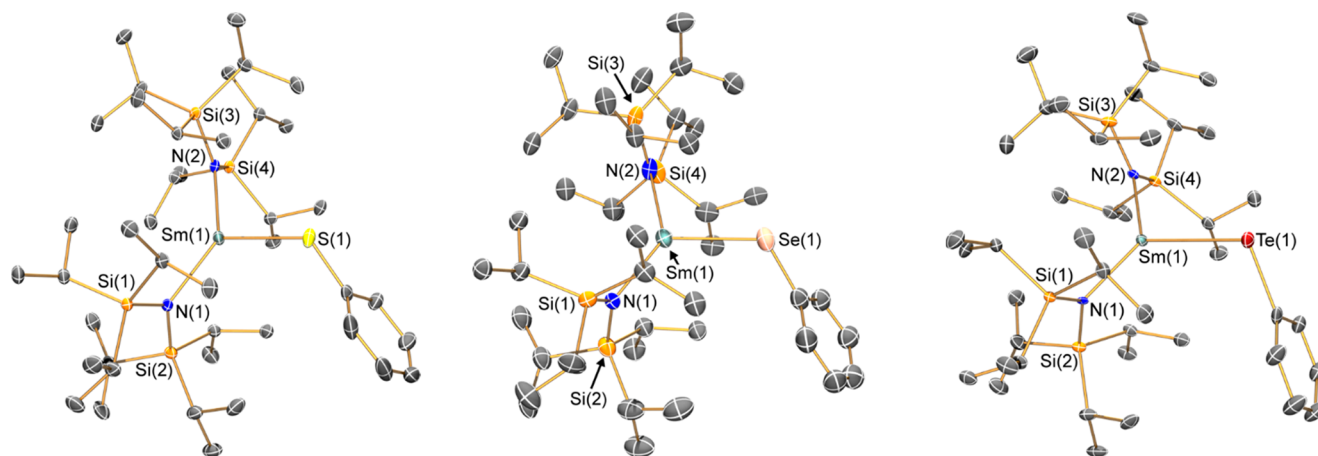
**Figure 2.** Molecular structures of $[Sm(N^{\dagger\dagger})_2(SPh)]$ (**1-S**, left), $[Sm(N^{\dagger\dagger})_2(SePh)]$ (**1-Se**, center), and $[Sm(N^{\dagger\dagger})_2(TePh)]$ (**1-Te**, right) with partial atom labeling. Displacement ellipsoids set at 30% probability level with hydrogen atoms are omitted for clarity.

**Table 2. Selected Bond Distances (Å) and Angles (deg) for 1-E**

|  | 1-S | 1-Se | 1-Te[a] |
|---|---|---|---|
| Sm−E | 2.6671(7) | 2.8458(10) | 3.1020(5) |
| Sm−N$_{avg}$ | 2.321(2) | 2.317(6) | 2.303(4) |
| N−Sm−N | 138.33(7) | 132.7(2) | 128.6(1) |
| N−Sm−E$_{avg}$ | 110.72(5) | 113.5(2) | 115.6(1) |
| Sm−E−C | 120.45(9) | 115.1(2) | 104.1(2) |
| Sm···N$_2$E$_{plane}$ | 0.065(1) | 0.074(3) | 0.082(2)[b] |

[a]Taken from molecule A in the asymmetric unit. [b]The Sm ion in molecule B resides 0.066(2) Å above the plane, thus the trend is not definitive.

**Table 3. Selected Bond Distances (Å) and Angles (deg) for 2-E$_2$**

|  | 2-S$_2$ | 2-Se$_2$ |
|---|---|---|
| Sm−E$_{avg}$ | 2.8394(7) | 2.9749(6) |
| Sm−N$_{avg}$ | 2.340(2) | 2.331(4) |
| E−E | 2.1075(10) | 2.3662(7) |
| Sm···Sm | 5.273(1) | 5.459(2) |
| Sm−E−Sm$_{avg}$ | 136.42(3) | 133.13(2) |
| Sm−E−E$_{avg}$ | 68.22(3) | 66.56(2) |
| E−Sm−E | 43.58(2) | 46.87(2) |
| $\alpha$[a] | 0.8(2) | 0.3(1) |
| $\theta$[b] | 45.8(1) | 45.3(1) |

[a]Dihedral angle between mean SmE$_2$ planes. [b]Dihedral angle between mean SmN$_2$ planes.

related compounds, the Ln···Ln separation is consistently below 5 Å, such that the distance in **2-S$_2$** represents the closest intermetallic separation permitted by the N$^{\dagger\dagger}$ ligand. We postulate that the considerable steric demands of N$^{\dagger\dagger}$ are responsible for analogous $\mu$-N$_2$ species being unknown to date and the formation of a Sm$_4$($\mu_3$-O)$_4$ cubane in $[\{Sm(N^{\dagger\dagger})_2\}_4(\mu_3$-O)$_4]$ (**5**) rather than $(\mu$-O$_2)^{-/2-}$ ligands. Complex **2-Se$_2$** has an analogous structure, though the larger Se atoms with greater p character produce more acute Sm−E−Sm angles (133.13(2)°) and larger E−Sm−E angles (66.56(2)°) than found in **2-S$_2$** (Table 3). The dimension of the strictly planar Sm$_2$Se$_2$ unit in **2-Se$_2$** is identical to that in $[\{Sm(Cp^*)_2\}_2(\mu$-

$\eta^2$:$\eta^2$-Se$_2$)],[50] where the Sm···Sm distance of 5.459(2) Å stems from the intrinsically longer Sm−Se bonds rather than the size of the coligand. In the structure of **2-Se$_2$**, there is a small disorder component (~2%) which contains the $\mu$-Se$^{2-}$ moiety; again this Sm−Se−Sm motif was first seen in Sm(III) chemistry from reactivity studies of $[Sm(Cp^*)_2(thf)_2]$.[35]

On one occasion, we obtained a polymorph of **2-S$_2$** that crystallized in a triclinic space group, which we include here as **2-S$_2$-polymorph** (Figure S2). The structural features of **2-S$_2$-polymorph** differ from **2-S$_2$** as it comprises two orientations of
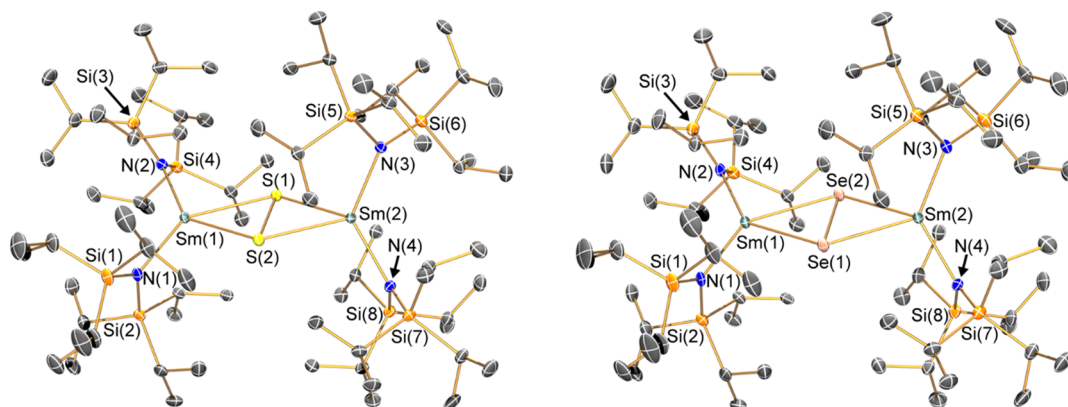


**Figure 3.** Molecular structures of $[\{Sm(N^{\dagger\dagger})_2\}_2(\mu$-$\eta^2$:$\eta^2$-S$_2$)]$ (**2-S$_2$**, left) and $[\{Sm(N^{\dagger\dagger})_2\}_2(\mu$-$\eta^2$:$\eta^2$-Se$_2$)]$ (**2-Se$_2$**, right) with partial atom labeling. Displacement ellipsoids set at 30% probability level, and hydrogen atoms are omitted for clarity.

the central $Sm_2S_2$ core with respect to the terminal $SmN_2$ moieties (Figure S3). The bond distances of **2-S$_2$-polymorph** are essentially identical to **2-S$_2$**, though the former exhibits a nearly parallel alignment of the two $SmN_2$ planes with $\theta = 4.6(1)°$ (cf. $45.8(1)°$ for **2-S$_2$**; Table S5).

In contrast to the diatomic bridges in **2-S$_2$** and **2-Se$_2$**, the Sm centers in complex **3** are linked by a $\mu$-Te ligand (Figure 4).



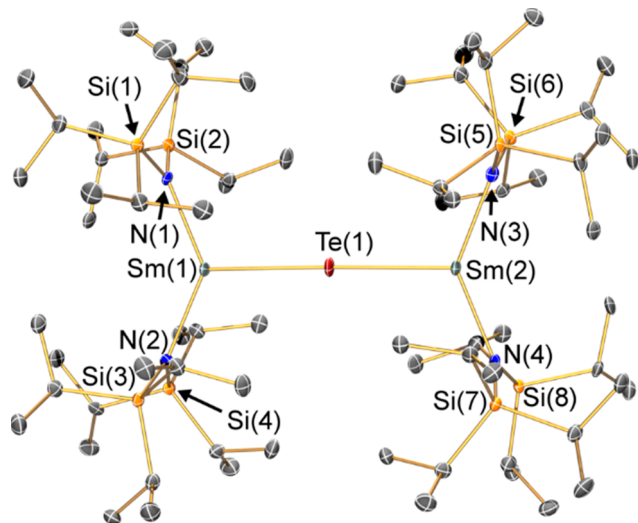**Figure 4.** Molecular structure of $[\{Sm(N^{\dagger\dagger})_2\}_2(\mu\text{-Te})]$ (**3**) with partial atom labeling. Displacement ellipsoids set at 30% probability level, and hydrogen atoms are omitted for clarity. Selected bond lengths: $Sm(1)-Te(1)$ 2.9485(5) Å, $Sm(2)-Te(1)$ 2.9461(5) Å, $Sm(1)-N(1)$ 2.314(5) Å, $Sm(1)-N(2)$ 2.327(5) Å, $Sm(2)-N(3)$ 2.325(5) Å, $Sm(2)-N(4)$ 2.334(5) Å, $Sm(1)\cdots Sm(2)$ 5.894(1) Å. Selected bond angles: $Sm(1)-Te(1)-Sm(2)$ 178.64(2)°, $N(1)-Sm(1)-N(2)$ 134.2(2)°, $N(3)-Sm(2)-N(4)$ 135.7(2)°.

The Sm–Te distances at 2.9461(5) and 2.9485(5) Å are not significantly different from the Sm–Se distances in **2-Se$_2$**, but the periodic trend with increasing chalcogen radius is observed in the Sm⋯Sm distance of 5.894(1) Å. Sm–Te–Sm complexes are rare, with $[\{Sm(Cp^*)_2(thf)\}_2(\mu\text{-Te})]$ being the only directly comparable complex;[35] its longer Sm–Te bond of 2.993(2) Å likely reflects the higher coordination number. The two $SmN_2$ planes in **3** are almost coplanar ($\theta = 6.4(1)°$), which results from crystal packing, as the same metric in **2-S$_2$** is $45.8(1)°$ but only $4.6(1)°$ in **2-S$_2$-polymorph** (Table S5). Changes in the canting in these moieties have been observed previously when bridging fragments get larger.[51]

**Electronic Spectroscopy.** Electronic absorption spectra of **1-E** and **2-E$_2$** were recorded as toluene solutions at ambient temperatures. The spectral overlay presented in Figure 5 highlights the similar profiles of the **1-E** series, which are dominated by a broad feature tailing in from the UV region. This results from ligand-to-metal charge transfer (LMCT) processes; each features an absorption maximum at ca. 26 000 cm$^{-1}$, which imbues **1-S** and **1-Se** with their yellow-orange hue. The slightly darker tone to **1-Te** stems from the additional peak at 18 150 cm$^{-1}$ with the spectral intensities trending **1-Te** > **1-S** > **1-Se**. All three complexes exhibit identical features in the NIR region, with two well-resolved sharp peaks at 7725 and 7710 cm$^{-1}$, and one broad peak with a shoulder in the range 8373−8395 cm$^{-1}$. These features are characteristic of $^6H_{5/2} \rightarrow {}^6F_{11/2,9/2,7/2}$ transitions based on comparisons with solid-state measurements of Ln(III) ions.[52] The spectrum of **2-**
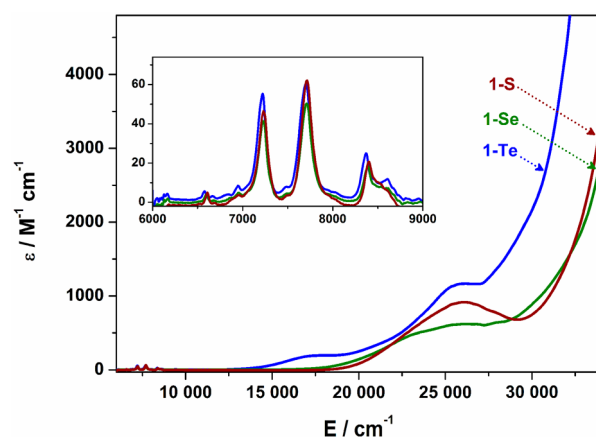


**Figure 5.** Overlay of the electronic spectra of **1-E** (E = S, Se, Te) as 1 mM solutions in toluene recorded at ambient temperature. Inset shows expansion of the NIR region.

**S$_2$** shows the same LMCT band at 26 000 cm$^{-1}$ and an additional peak at 21 000 cm$^{-1}$ (Figure S60). The fingerprint profile in the NIR shows the same three bands as for the **1-E** series, although slightly blue-shifted, suggesting an identical coordination geometry for the two Sm(III) ions in **2-S$_2$**. On the other hand, **2-Se$_2$** possesses a featureless envelope of LMCT transitions in the range 21 000−29 000 cm$^{-1}$ but a sharper suite of fingerprint transitions that are red-shifted by ∼200 cm$^{-1}$ (Figure S60). This profile likely stems from the presence of two Sm(III) ions with slightly different coordination geometry given the increased flexibility of the coordination sphere, which is not beholden to intramolecular interactions of the $N^{\dagger\dagger}$ coligands.

**X-ray Absorption Spectroscopy.** The electronic structures of **1-S**, **2-S$_2$**, and **2-Se$_2$** were examined using X-ray absorption spectroscopy (XAS) at the Sm L$_3$-edge. With a measurement energy of ca. 6720 eV, these spectra are not affected by electronic effects inherent to highly anisotropic ions that complicate many other techniques. The L$_3$-edge spectrum is dominated by a white-line peak composed of dipole-allowed 2p → 6s and 2p → 5d transitions.[53] For Ln ions with valence electrons residing in the 4f-subshell, dipole forbidden but quadrupole-allowed 2p → 4f electronic transitions constitute the pre-edge region at the base of the white-line peak.[54] These features are rarely observed in transmission experiments as they are buried beneath the white line, therefore we utilize fluorescence-detection to resolve the pre-edge peaks. Experimental spectra are compared in Figure 6, and pre-edge and white-line energies and intensities are listed in Table 4. The white-line energies across the series are essentially invariant, falling into the range 6722.7 ± 0.1 eV, with **2-S$_2$** and **2-Se$_2$** at slightly higher energies. These energies are identical to Sm L$_3$-edge energies recorded for related series $[Sm(N^{\dagger\dagger})_2X]$ (X = F, Cl, Br, I), which ranged 6722.5−6723.1 eV.[26] The enhanced resolution of the L$\alpha_1$ fluorescence spectrum yielded resolved pre-edge features for each compound, manifesting as two shoulder peaks at the base of the white line (Figure 6 inset). The first pre-edge is shifted 0.4 eV to higher energy for **2-Se$_2$** following the observation of higher energy with increasing size of the donor atom;[26,55] the second peak is constant at 6716.1 ± 0.1 eV. The pre-edge peaks reside ca. 10 eV below the white line, similar to the halide series,[26] as well as high-resolution studies performed on $Ce_2(CO_3)_3$ at 8.5 eV and $Yb_2O_3$ at 10.2 eV, to select two elements at either end of the Ln series.[56]
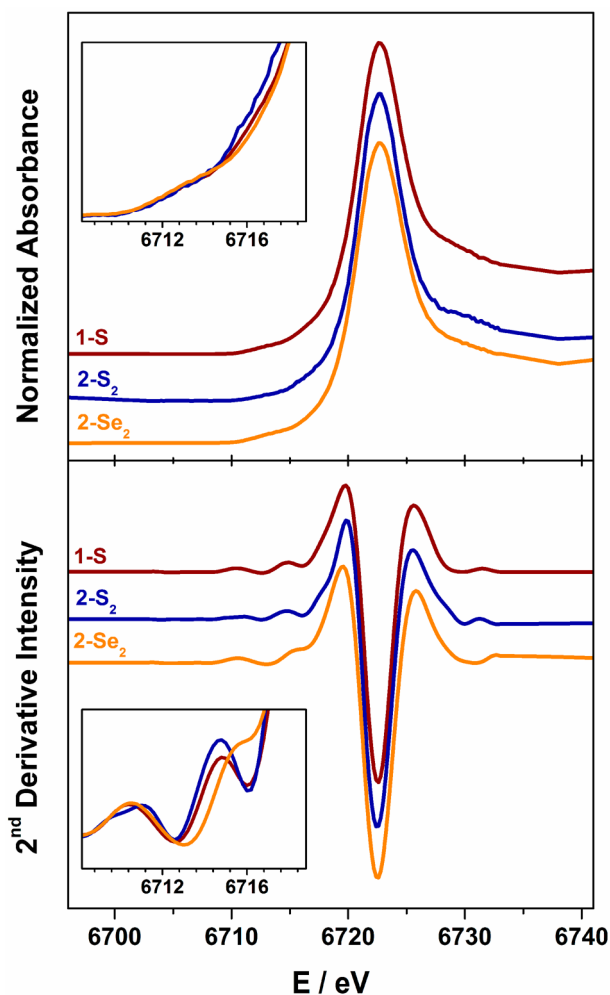
E

**Figure 6.** Comparison of the normalized Sm L$_3$-edge XAS (top) and their FFT-smoothed second derivative spectra (bottom) for **1-S**, **2-S$_2$**, and **2-Se$_2$** recorded at 100 K. Insets show expansion of the overlaid FFT-smoothed pre-edge peak (top) and their second derivative (bottom).

**Theoretical Calculations.** *Ground State Electronic Structure.* Our previous study on low-coordinate Sm(III) complexes utilized a simple time-dependent (TD) DFT method to reproduce the experimental X-ray absorption spectra.[26,57] Typically, this approach has been used to evaluate covalency in a suite of d-block complexes,[4,18,19,58] but the contracted 4f-subshell renders a similar quantification in lanthanide complexes unattainable. However, reproduction of the L$_3$-edge spectrum measured the spin polarization at these paramagnetic centers, i.e., the difference in energy between $\alpha$-

spin (spin-up) and $\beta$-spin (spin-down) 4f orbitals, as well as the position of the 5d manifold. Using the Sm L$_3$-edge spectrum of **1-S** as a reference point, we screened a suite of functionals and basis sets to select the best combination that match the experiment. Calculation of the L$_3$-edge spectrum of **1-S** was carried out on the crystallographic coordinates of the molecule. For a given theoretical method—functional and basis set—an empirical correction is applied to the calculated Sm L$_3$-edge spectrum to align it with the experimental data highlighting the effect of the calculation parameters on the ground state electronic structure.[57,59] The chosen functionals PBE,[60] $\omega$B97-X,[61] PBE0,[62] BHandHLYP,[63] and M062X[64] are listed in order of increasing Hartree–Fock (HF) exchange of 0%, 16%, 25%, 50%, and 54%, respectively.

A comparison of the calculated Sm L$_3$-edge was made with the bespoke segmented all-electron relativistically contracted (SARC) basis set for Sm.[65] This compact basis set was used for the calculation of the corresponding halide series $[\text{Sm}(\text{N}^{\dagger\dagger})_2\text{X}]$ (X = F, Cl, Br, I) and underestimated the 4f–5d energy gap by 4 eV with the PBE0 functional.[26] With the SARC-ZORA-TZVP basis set, the BHandHLYP functional gave the best match, with a pre-edge splitting of 4.5 eV and first pre-edge peak position 11.2 eV below the white line (Figure S69). Overall, the PBE0/ZORA-def2-TZVPP combination gave the best result and was applied to the calculation of the Sm L$_3$-edge of **2-S$_2$** and **2-Se$_2$**. For these compounds, the calculated spectra were normalized and overlaid with that of **1-S** (Figure 7). Overall, the calculated spectra are in very good agreement with the experiment, with the relative energy and relative intensity of the two pre-edge peaks well reproduced (Table 4). Where the calculated spectrum diverges from the experimental one above 6716 eV marks the start of the dominant white-line peak whose line width differs from the pre-edge features and is difficult to model with the uniform line width and Gaussian line shape output from the calculations.

The performance of each functional was assessed by the splitting of the two pre-edge peaks and their position relative to the white line. The most accurate reproduction was achieved with the PBE0 hybrid functional (25% HF), with a pre-edge splitting energy of 2.9 eV and first pre-edge peak position 9.0 eV below the white line compared with the experimental values of 3.4 and 10.0 eV, respectively (Table 4). The remaining functionals followed the trend of increasing energy splitting with increasing HF exchange (Table S7). The improved resolution provided by detection of the L$\alpha_1$ fluorescence line gave two well-defined pre-edge peaks that result almost entirely from quadrupole-allowed 2p → 4f transitions. The first comprises the excitation of a spin-up electron to the two unoccupied f orbitals in the $\alpha$-spin manifold with probability density projected toward the ligands. The second peak

**Table 4. Experimental and Calculated Sm L$_3$-edge XAS Data**[a]

| | pre-edge[b] | | intensity[c] | white-line[b] | | intensity[d] |
|---|---|---|---|---|---|---|
| **1-S** | 6712.6 | (6713.6) | 0.08 | 6722.6 | (6722.6) | 10.8 |
| | 6716.0 | (6716.5) | 0.27 | | | |
| **2-S$_2$** | 6712.6 | (6713.4) | 0.07 | 6722.7 | (6722.7) | 14.6 |
| | 6716.1 | (6716.3) | 0.32 | | | |
| **2-Se$_2$** | 6713.0 | (6713.4) | 0.10 | 6722.8 | (6722.7) | 10.5 |
| | 6716.2 | (6716.3) | 0.27 | | | |

[a]Calculated (PBE0/def2-TZVPP) values in parentheses are shifted −193.6 eV. [b]Energy of minimum in second derivative spectrum. [c]Pre-edge peak height, in arbitrary units. [d]Area under the single Gaussian fit to the white-line peak after subtraction of the edge, in arbitrary units.
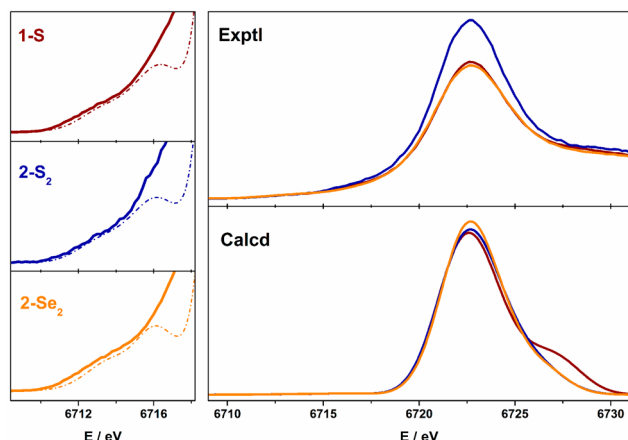
**Figure 7.** Comparison of the experimental (top) and calculated (bottom) Sm $L_3$-edge spectra for **1-S** (red), **2-S$_2$** (blue), and **2-Se$_2$** (orange) obtained from PBE0/ZORA-def2-TZVPP TD-DFT calculations. Calculated spectra are shifted −193.6 eV with a 3 eV line broadening. The left panel shows expansion of the pre-edge region with the solid line depicting the experimental data and the dashed line, the calculated pre-edge spectrum. Calculated stick plot spectra are shown in Figures S70−S72.

comprises excitations to the seven unoccupied $\beta$-spin f orbitals of the Sm(III) ion (Figures S70−S72). The difference in energy of the two pre-edge peaks is a measure of the polarization of the valence orbitals, which stabilizes the $\alpha$-spin f orbitals relative to their $\beta$-spin counterparts by 3.4, 3.5, and 3.2 eV in **1-S**, **2-S$_2$**, and **2-Se$_2$**, respectively (Table 4). This effect also manifests in the Mulliken spin population analysis leading to more than five unpaired spins at the Sm ion, which increases with increasing size of the chalcogen (Figure S73). This is

brought about by a poorer energy match of the 4f-manifold with the $n$p orbitals of the chalcogen such that Se 4p and Te 5p orbitals are energetically closer to the Sm 5d orbitals.[28,46,66]

*Exchange Coupling via Bridging Radicals.* The potential of dichalcogenide radicals to mediate exchange interactions within dilanthanide complexes can be measured by the magnitude of their isotropic exchange coupling constants ($J$), as defined by the spin-Hamiltonian shown in eq 1. Broken symmetry DFT calculations have proven effective at estimating the Ln−radical ($J_{ex}$) and Ln−Ln ($J'_{ex}$) coupling constants in the $[\{Ln(N'')_2(thf)\}_2(\mu-\eta^2:\eta^2-N_2)]^-$ (Ln = Gd, Tb, Dy, Ho, Er) series,[13,67,68] especially for the anisotropic ions where such parameters are difficult to measure experimentally, including Sm. The difference in the total energies for the high-spin (HS) and broken symmetry (BS) electronic solutions gives reliable estimates for $J_{ex}$ and $J'_{ex}$ using the preferred nonspin-projected approach defined in eqs 2 and 3.[69] The veracity of this method was calibrated for the gadolinium species as the $^8$S ion is devoid of contributions from spin−orbit coupling.[13,67,68] The experimentally validated PBE0/ZORA-def2-TZVPP protocol was used to calculate the ground state electronic structures of **2-S$_2$** and their one-electron oxidized and reduced species. The computed $J$ values are benchmarked by comparing to those calculated for $[\{Gd(N'')_2(thf)\}_2(\mu-\eta^2:\eta^2-N_2)]$ and $[\{Gd(N'')_2(thf)\}_2(\mu-\eta^2:\eta^2-N_2)]^-$. Using our theoretical procedure, we have calculated the exchange coupling between the Gd(III) ions in $[\{Gd(N'')_2(thf)\}_2(\mu-\eta^2:\eta^2-N_2)]$ at $J'_{ex} = -0.32$ cm$^{-1}$, which is a good match to the experimental value of −0.49 cm$^{-1}$[10] and similar to other DFT-derived estimates (−0.53 cm$^{-1}$ and −0.33 cm$^{-1}$).[67,68] Such a miniscule value reflects the large separation between the Gd(III) ions such that they are uncoupled paramagnetic centers.
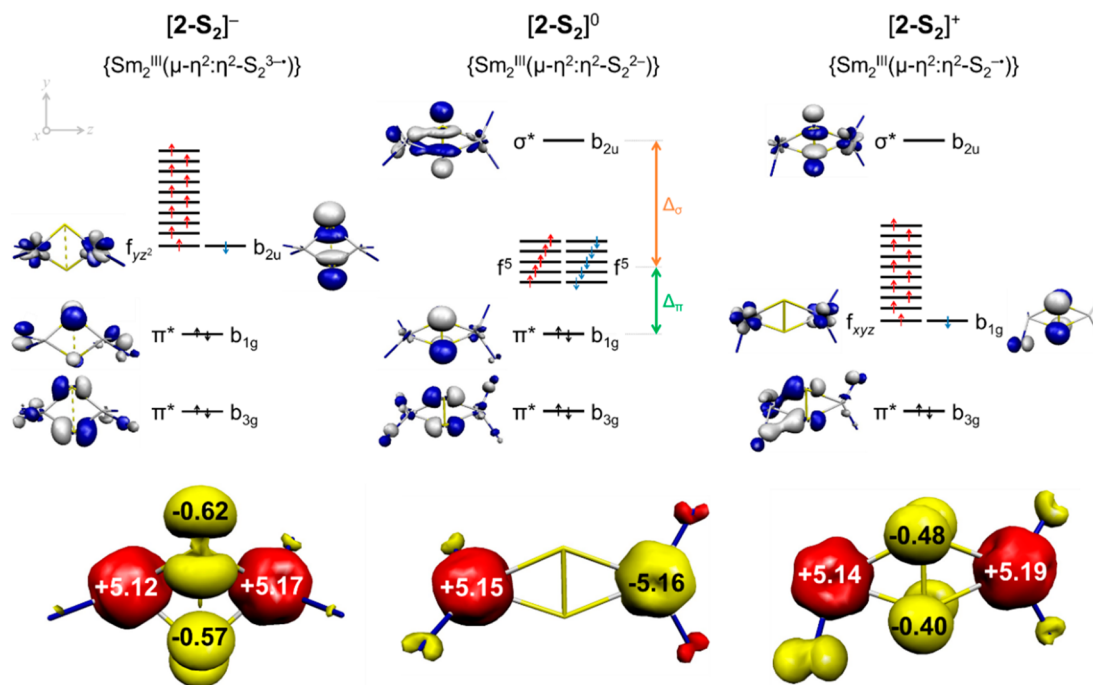


**Figure 8.** Qualitative MO scheme for the $[2\text{-}S_2]^{-/0/+}$ electron transfer series showing relative energies of the frontier orbitals derived from DFT calculations. Singly occupied MOs are denoted with red and blue arrows for $\alpha$-spin and $\beta$-spin electrons, respectively. $\Delta_\sigma$ and $\Delta_\pi$ are the energy gaps between the 4f manifold and the ligand-based $\sigma^*$ ($b_{2u}$) and $\pi^*$ ($b_{1g}$) MOs, respectively (in $D_{2h}$ symmetry). Below are presented the Mulliken spin population analyses (red, $\alpha$-spin; yellow, $\beta$-spin).

G

$$\hat{H} = -2J_{ex}\hat{S}_L \cdot (\hat{S}_{Sm1} + \hat{S}_{Sm2}) - 2J'_{ex}\hat{S}_{Sm1} \cdot \hat{S}_{Sm2} \qquad (1)$$

$$J_{ex} = (E_{BS1} - E_{HS})/12 \qquad (2)$$

$$J'_{ex} = [(E_{BS2} - E_{BS1}) + 2J_{ex}]/30 \qquad (3)$$

Geometry optimization of **2-S$_2$** and **2-Se$_2$** was started from their crystallographic coordinates. The bulky N$^{\dagger\dagger}$ ligands were trimmed to the N″-sized variant in order to speed up the calculations. These simplified structures do not significantly alter the underlying electronic structure like the ground state electronic structure as measured by orbital energies and composition, and overlap integrals of the paramagnetic centers are unchanged. There are noticeable differences in the geometries, which is a consequence of lifting the steric demands of the N$^{\dagger\dagger}$ ligands in these truncated models (see SI for details). The ground state electronic structures of **2-S$_2$** and **2-Se$_2$** models were computed at the PBE0/ZORA-def2-TZVPP level of DFT. A broken-symmetry BS(5,5) calculation gives five $\alpha$-spin SOMOs on one Sm(III) ion and five corresponding $\beta$-spin SOMOs on the other Sm(III) ion (Figure 8). The large intermetal separation ensures there is no overlap of magnetic orbitals, with the overlap integral S ≈ 0. The 4f orbitals are nestled between the two occupied $\pi$* MOs of the disulfide, which transform as b$_{3g}$ and b$_{1g}$ in D$_{2h}$ symmetry, and the unoccupied $\sigma$* (b$_{2u}$) MO, which confers a bond order of 1. The Mulliken spin population analysis gives more than five spins at Sm due to the aforementioned spin polarization.

The Sm–Sm exchange coupling constants ($J'_{ex}$) in **2-S$_2$** and **2-Se$_2$** are estimated at −0.94 and −0.71 cm$^{-1}$, respectively. The coupling is slightly larger than the corresponding value computed for [{Gd(N″)$_2$(thf)}$_2$($\mu$-$\eta^2$:$\eta^2$-N$_2$)] ($J'_{ex}$ = −0.32 cm$^{-1}$), indicating a slightly more efficient superexchange pathway is produced by larger donor atoms. Interestingly, $J'_{ex}$ calculated on the solid state structures of **2-S$_2$** and **2-Se$_2$** is smaller in magnitude and weakly ferromagnetic, with values of +0.54 and +0.07 cm$^{-1}$, respectively. We ascribe this difference to the nonplanarity of the Sm$_2$E$_2$ unit in the optimized structures giving shorted Sm–E and Sm···Sm distances than in the solid state. The distortion of the diamond core has been shown to induce a positive shift in the exchange coupling constant,[67] though we note a shift of ca. 1 cm$^{-1}$ is largely insignificant.

The addition of an electron to the **2-S$_2$** model generates a monoanionic compound with two Sm(III) ions linked through a bridging subsulfide, (S$_2$)$^{3−\bullet}$. The locus of the redox event is clearly indicated by the lengthening of the S···S distance to 3.254 Å, commensurate with a two-center/three-electron bond.[17] Berry and co-workers have catalogued all structurally characterized compounds with subsulfide ligands and showed for second and third row d-block metals that the S···S distance ranges from 2.9–3.1 Å.[19] Although the S···S distance in the [**2-S$_2$**]$^−$ model lies just outside this interval, it is shorter than the nonbonded sulfide distance of over 3.5 Å in [{Zr(Cp)$_2$}$_2$($\mu$-S)$_2$].[70] The Sm···Sm separation decreases by ca. 1 Å as the fold along the S···S vector increases to 40.5° (Table S15). The decrease in the intermetal separation is diagnostic of ligand-centered reduction as the Sm–S–Sm angle approaches 90° in order to accommodate the shorter Sm–S distance driven by electrostatic attraction with the trianionic bridging ligand. Therefore, the bulk of the N$^{\dagger\dagger}$ ligands is likely preventing the formation of the monoanionic species by restricting the Sm

ions from adopting a disposition that stabilizes the bridging subsulfide group. This observation is in line with the current absence of any Ln$_2$($\mu$-$\eta^2$:$\eta^2$-N$_2$) compound with N$^{\dagger\dagger}$, hence N″ ligands are necessary to achieve convergence of the optimized [**2-S$_2$**]$^−$ species. A BS(10,1) calculation revealed that the $M_S$ = $^9/_2$ state (identified as BS1) is 1.5 kcal mol$^{-1}$ more stable than the high-spin (HS) solution. This ground state consists of parallel alignment of the 10 unpaired electrons from the Sm(III) ions that are antiferromagnetically coupled to the unpaired spin of the subsulfide (Figure 8). The reduced ligand, although bearing the same charge as the dinitrogen analogues, has its unpaired electron in a $\sigma$* (b$_{2u}$) MO, in contrast to the $\pi$* (b$_{1g}$) SOMO in (N$_2$)$^{3−\bullet}$.[13,67,68] The alternative scenario is antiferromagnetic coupling between terminal Sm(III) ions leading to a net $M_S$ = $^1/_2$ state (denoted BS2). Addition of an electron to the ligand creates a $\sigma$* SOMO which has a small overlap (S = 0.17) with the corresponding magnetic orbital in the $\alpha$-spin manifold being the f$_{yz^2}$ orbital (Table 5). Although

**Table 5. Calculated Exchange Coupling Constants ($J$/cm$^{-1}$), Energy Gaps ($\Delta$/cm$^{-1}$), and Orbital Overlap Integrals (S)**

| | [2-S$_2$]$^−$ | 2-S$_2$ | [2-S$_2$]$^+$ | [2-Se$_2$]$^−$ | 2-Se$_2$ |
|---|---|---|---|---|---|
| $J_{ex}$ [a] | −33.9 | | −44.1 | −33.9 | |
| $J'_{ex}$ [b] | +7.0 | −0.94 | +4.0 | +1.7 | −0.71 |
| $\Delta_\sigma$ | 8100 | 33 500 | 36 300 | 9470 | 30 600 |
| $\Delta_\pi$ | 2240 | 4130 | 1400 | 2100 | 5690 |
| S | 0.17 | ~0 | 0.14 | 0.14 | ~0 |

[a] Sm−radical exchange coupling constant. [b] Sm−Sm exchange coupling constant.

the exchange interaction is larger than calculated for the (N$_2$)$^{3−\bullet}$ series,[67,68] it is relatively weak, with largely electrostatic bonding given the 82% S 3p character in this $\beta$-spin SOMO (Table S21). The composition of the $\sigma$* MO is unchanged from the neutral complex and consistent with bond covalency derived from E $n$p−Ln 5d overlap.[71] The Mulliken spin analysis locates more than five spins on each Sm(III) ion and more than one spin on the subsulfide unit.

Using total energies for the HS, BS1, and BS2 states, the Sm−radical and Sm−Sm exchange coupling constants for the [**2-S$_2$**]$^−$ model are estimated at −33.9 cm$^{-1}$ and +7.0 cm$^{-1}$, respectively. Considering the aforementioned functional and basis set dependency for calculated parameters, we calculated the corresponding parameters for [{Gd(N″)$_2$(thf)}$_2$($\mu$-$\eta^2$:$\eta^2$-N$_2$)]$^−$ at $J_{ex}$ = −35.2 cm$^{-1}$ and $J'_{ex}$ = +2.9 cm$^{-1}$. There is good agreement with the experimental $J_{ex}$ value of −27 cm$^{-1}$, though the $J'_{ex}$ value is overestimated given the experimental result of −0.49 cm$^{-1}$.[10] Comparing the two bridging ligands, (S$_2$)$^{3−\bullet}$ and (N$_2$)$^{3−\bullet}$, the $J_{ex}$ values are the same but the $J'_{ex}$ coupling is twice the magnitude for the subsulfide ligand. This follows the trend observed for the nonradical (S$_2$)$^{2−}$ ligand with the analogous (N$_2$)$^{2−}$ species (vide supra). The salient difference provided by the dichalcogenido bridge and the (N$_2$)$^{3−\bullet}$ analogues is the small energy gap ($\Delta_\sigma$) between the corresponding magnetic orbitals being an order of magnitude smaller for the [**2-S$_2$**]$^−$ model. This has the effect of supplying a greater contribution from promotion energy of electron transfer to the exchange interaction because the paramagnetic ions more efficiently overlap through the dichalcogenide ligand.[13] This offsets the diminished contribution from direct exchange, and delocalization of unpaired electrons (i.e., covalency) of the larger Sm$_2$S$_2$ core. The bond metrics in

the optimized structure of the one-electron reduced Se-containing model, $[\mathbf{2}\text{-}\mathbf{Se_2}]^-$, are quite similar to those of the $[\mathbf{2}\text{-}\mathbf{S_2}]^-$ model (Table S15). The reduction occurs at the bridging $\mathrm{Se_2}$ ligand, with a pronounced lengthening of the bond to 3.546 Å, which again falls in the range for subselenide ligands,[17−19] and within the van der Waals radius for $\mathrm{Se_2}$.[72] The calculated exchange coupling constants are slightly smaller than for $[\mathbf{2}\text{-}\mathbf{S_2}]^-$, a consequence of the larger $\mathrm{Sm_2Se_2}$ core.

Dichalcogenide ligands can also be oxidized to the $(\mathrm{E_2})^{-\bullet}$ redox level that is also paramagnetic.[17−19] The optimized structure of the $[\mathbf{2}\text{-}\mathbf{S_2}]^+$ model gave a S−S bond distance of 2.149 Å, which is longer than observed experimentally for $\mathbf{2}\text{-}\mathbf{S_2}$ but shorter than in the optimized neutral compound (Table S15). This is consistent with an increase in the bond order to form a supersulfide group. In contrast, optimization of the oxidized $\mathbf{2}\text{-}\mathbf{Se_2}$ model failed to converge, highlighting the reluctance of Se to multiply bond with itself.[73] The ligand-based SOMO is the $b_{1g}$ $\pi^*$ orbital, which antiferromagnetically couples to a metal-based SOMO of matching symmetry composed of the $f_{xyz}$ orbital of each Sm(III) ion (Figure 8). The overlap integral (S = 0.14) is marginally smaller than for the $[\mathbf{2}\text{-}\mathbf{S_2}]^-$ model and suggests that the anticipated increase in overlap provided by the Se 4p orbitals is counteracted by the larger spatial separation of the paramagnetic centers. Hence, the $(\mathrm{S_2})^{3-\bullet}$ ligand in $[\mathbf{2}\text{-}\mathbf{S_2}]^-$ is more effective at penetrating the 4f orbitals because of its extra (negative) charge. This is best seen in the Mulliken spin population of $[\mathbf{2}\text{-}\mathbf{S_2}]^+$ with more than five spins at each Sm ion but only −0.88 spins on the bridging sulfur atoms, where the bond polarization shifts to the nitrogen donors of the N″ ligands (Figure 8). The S−S $\pi^*$ SOMO has only 68.4% 3p content, with a further reduction in the Sm 4f and 5d contribution compared with the $\sigma^*$ SOMO (Table S21). However, it is much closer in energy to the 4f manifold, with a separation $\Delta_\pi$ = 1400 $\mathrm{cm^{-1}}$ making the electron transfer process more facile. Despite the larger dimension, the calculated exchange constant of $J_{ex}$ = −44.1 $\mathrm{cm^{-1}}$ is a third larger than that calculated for the $[\mathbf{2}\text{-}\mathbf{S_2}]^-$ model (Table 5). This may suggest that a more efficient exchange pathway is provided by a $\pi$ radical compared with a $\sigma$ radical, although $J'_{ex}$ is half the size and a consequence of the larger intermetallic separation in $[\mathbf{2}\text{-}\mathbf{S_2}]^+$. Any electronic influence on this distortion exerted by the core atoms would be very small and easily overridden by the steric demands of the coligands and coordination environment of the Sm ion.

## CONCLUSIONS

The single-electron transfer chemistry of $[\mathrm{Sm}(\mathrm{N}^{\dagger\dagger})_2]$ has been utilized to produce a suite of mono- and dinuclear chalcogen complexes. This redox chemistry should be transferable to a wide range of Ln(II) and Ln(III) reduced dinitrogen complexes, and the nuclearity of the products can be easily tuned by subtle variations in ligand sterics. These structurally homologous families of complexes have been examined by Sm $\mathrm{L_3}$-edge XAS, where the fluorescence detection method provides well resolved pre-edge and white-line features. The straightforward TD-DFT protocol developed previously for Sm $\mathrm{L_3}$-edge spectra was successfully used to reproduce the key spectral features. The experimentally validated protocol was applied to the calculation of the ground state electronic structure of models of $\mathbf{2}\text{-}\mathbf{E_2}$. One-electron oxidation and reduction of $\mathbf{2}\text{-}\mathbf{S_2}$ is ligand-centered. Oxidation gave a bridging supersulfide in $[\mathbf{2}\text{-}\mathbf{S_2}]^+$, and reduction gave a subsulfide in $[\mathbf{2}\text{-}\mathbf{S_2}]^-$. On the other hand, only the reduced $\mathbf{2}\text{-}\mathbf{Se_2}$ species is

calculated to be stable. The exchange interaction provided by these contrasting $\sigma$- and $\pi$-radical ligands was assessed by the magnitude of the calculated exchange coupling constants, which showed that the $\pi$ SOMO in the supersulfide produced the strongest Sm−radical coupling, but the $\sigma$ SOMO in the subsulfide gave the larger Sm−Sm exchange interaction. These $J_{ex}$ values are roughly equivalent to those in benchmark $(\mathrm{N_2})^{3-\bullet}$ bridged species, but both $[\mathbf{2}\text{-}\mathbf{S_2}]^+$ and $[\mathbf{2}\text{-}\mathbf{S_2}]^-$ models gave superior $J'_{ex}$ values, highlighting the advantage of larger donor atoms. Therefore, dichalcogenides, in particular the radicals of disulfide, could be potential successors to their dinitrogen counterparts. Their application to chemical systems pertinent to molecular magnetism requires addressing an important design criterion, namely the coligand. Although the significant bulk of $\mathrm{N}^{\dagger\dagger}$ is advantageous in stabilizing exotic near-linear Ln(II) and bent Ln(III) species,[24,25,30] its size hinders subsequent redox activation of the dichalcogenide bridging ligand. This impediment becomes more acute with the magnetically popular Ln ions with smaller ionic radii.[6] This obstacle is circumvented by scaling the size of the coligand to match the f-element, where bis(silyl)amides present an almost limitless range of options.[43,74] An alternative strategy is a shift to An, which not only eliminates the coligand dependency[44] but the more diffuse 5f-orbitals offers greater covalency and potentially stronger magnetic coupling.[9] We anticipate that such studies could provide molecular magnets with monstrous exchange interactions, together with rich information on 4f vs 5f covalency.

## ASSOCIATED CONTENT

### Ⓢ Supporting Information

The Supporting Information is available free of charge at https://pubs.acs.org/doi/10.1021/acs.inorgchem.0c00470.

> Syntheses, crystallography, molecular structures of **2-S2-polymorph** and **4−7**, NMR spectroscopy, VT NMR spectroscopy, magnetometry, cyclic voltammetry, electronic spectroscopy, FTIR spectroscopy, X-ray absorption spectroscopy, and density functional theoretical calculations (PDF)

### Accession Codes

CCDC 1945230−1945240 contain the supplementary crystallographic information for this paper. These data can be obtained free of charge via www.ccdc.cam.ac.uk/data_request/cif, or by emailing data_request@ccdc.cam.ac.uk, or by contacting The Cambridge Crystallographic Data Centre, 12 Union Road, Cambridge CB2 1EZ, UK; fax: + 44 1223 336033.

## AUTHOR INFORMATION

### Corresponding Authors

**David P. Mills** − *School of Chemistry, The University of Manchester, Manchester M13 9PL, United Kingdom;* ⓞ orcid.org/0000-0003-1575-7754; Email: david.mills@manchester.ac.uk

**Stephen Sproules** − *WestCHEM, School of Chemistry, University of Glasgow, Glasgow G12 8QQ, United Kingdom;* ⓞ orcid.org/0000-0003-3587-0375; Email: stephen.sproules@glasgow.ac.uk

## Authors

**Conrad A. P. Goodwin** − *School of Chemistry, The University of Manchester, Manchester M13 9PL, United Kingdom;* ○ orcid.org/0000-0002-4320-2548

**Benjamin L. L. Réant** − *School of Chemistry, The University of Manchester, Manchester M13 9PL, United Kingdom*

**Gianni F. Vettese** − *School of Chemistry, The University of Manchester, Manchester M13 9PL, United Kingdom*

**Jon G. C. Kragskow** − *School of Chemistry, The University of Manchester, Manchester M13 9PL, United Kingdom*

**Marcus J. Giansiracusa** − *School of Chemistry, The University of Manchester, Manchester M13 9PL, United Kingdom*

**Ida M. DiMucci** − *Department of Chemistry and Chemical Biology, Baker Laboratory, Cornell University, Ithaca, New York 14853, United States;* ○ orcid.org/0000-0003-3440-7856

**Kyle M. Lancaster** − *Department of Chemistry and Chemical Biology, Baker Laboratory, Cornell University, Ithaca, New York 14853, United States;* ○ orcid.org/0000-0001-7296-128X

Complete contact information is available at:
https://pubs.acs.org/10.1021/acs.inorgchem.0c00470

## Notes

The authors declare no competing financial interest.

## ■ REFERENCES

(1) Jensen, W. B. *The Lewis Acid-Base Concepts: An Overview*; Wiley: New York, 1980.

(2) (a) Li, H.-X.; Zhu, Y.-J.; Cheng, M.-L.; Ren, Z.-G.; Lang, J.-P.; Shen, Q. Lanthanide Chalcogenolate Complexes: Synthesis, Structures and Applications in Organic Chemistry. *Coord. Chem. Rev.* **2006**, *250*, 2059. (b) Nief, F. Complexes Containing Bonds Between Group 3, Lanthanide or Actinide Metals and Non-First-Row Main Group Elements (Excluding Halogens). *Coord. Chem. Rev.* **1998**, *178−180*, 13.

(3) (a) Brennan, J. G. In *The Rare Earth Elements: Fundamentals and Applications*; Atwood, J. L., Ed.; John Wiley & Sons Ltd: Chichester, 2012; p 215. (b) Zhou, J. Synthesis of Heterometallic Chalcogenides Containing Lanthanide and Group 13−15 Metal Elements. *Coord. Chem. Rev.* **2016**, *315*, 112.

(4) Daly, S. R.; Keith, J. M.; Batista, E. R.; Boland, K. S.; Clark, D. L.; Kozimor, S. A.; Martin, R. L. Sulfur K-edge X-ray Absorption Spectroscopy and Time-Dependent Density Functional Theory of Dithiophosphinate Extractants: Minor Actinide Selectivity and Electronic Structure Correlations. *J. Am. Chem. Soc.* **2012**, *134*, 14408.

(5) Lewis, F. W.; Hudson, M. J.; Harwood, L. M. Development of Highly Selective Ligands for Separations of Actinides from Lanthanides in the Nuclear Fuel Cycle. *Synlett* **2011**, *2011*, 2609.

(6) Rinehart, J. D.; Long, J. R. Exploiting Single-Ion Anisotropy in the Design of f-Element Single-Molecular Magnets. *Chem. Sci.* **2011**, *2*, 2078.

(7) Woodruff, D. N.; Winpenny, R. E. P.; Layfield, R. A. Lanthanide Single Molecule Magnets. *Chem. Rev.* **2013**, *113*, 5110.

(8) Guo, F.-S.; Bar, A. K.; Layfield, R. A. Main Group Chemistry at the Interface with Molecular Magnetism. *Chem. Rev.* **2019**, *119*, 8479.

(9) Liddle, S. T.; van Slageren, J. Improving f-Element Single Molecule Magnets. *Chem. Soc. Rev.* **2015**, *44*, 6655.

(10) Rinehart, J. D.; Fang, M.; Evans, W. J.; Long, J. R. Strong Exchange and Magnetic Blocking in $N_2^{3-}$-Radical-Bridged Lanthanide Complexes. *Nat. Chem.* **2011**, *3*, 538.

(11) Rinehart, J. D.; Fang, M.; Evans, W. J.; Long, J. R. A $N_2^{3-}$ Radical-Bridged Terbium Complex Exhibiting Magnetic Hysteresis at 14 K. *J. Am. Chem. Soc.* **2011**, *133*, 14236.

(12) Demir, S.; Gonzalez, M. I.; Darago, L. E.; Evans, W. J.; Long, J. R. Giant Coercivity and High Magnetic Blocking Temperatures for $N_2^{3-}$ Radical-Bridged Dilanthanide Complexes upon Ligand Dissociation. *Nat. Commun.* **2017**, *8*, 2144.

(13) Vieru, V.; Iwahara, N.; Ungur, L.; Chibotaru, L. F. Giant Exchange Interaction in Mixed Lanthanides. *Sci. Rep.* **2016**, *6*, 24046.

(14) (a) Demir, S.; Jeon, l.-R.; Long, J. R.; Harris, T. D. Radical Ligand-Containing Single-Molecule Magnets. *Coord. Chem. Rev.* **2015**, *289−290*, 149. (b) Demir, S.; Zadrozny, J. M.; Nippe, M.; Long, J. R. Exchange Coupling and Magnetic Blocking in Bipyrimidyl Radical-Bridged Dilanthanide Complexes. *J. Am. Chem. Soc.* **2012**, *134*, 18546.

(15) (a) Hua, C.; DeGayner, J. A.; Harris, T. D. Thiosemiquinoid Radical-Bridged $Cr^{III}_2$ Complexes with Strong Magnetic Exchange Coupling. *Inorg. Chem.* **2019**, *58*, 7044. (b) Tuna, F.; Smith, C. A.; Bodensteiner, M.; Ungur, L.; Chibotaru, L. F.; McInnes, E. J. L.; Winpenny, R. E. P.; Collison, D.; Layfield, R. A. A High Anisotropy Barrier in a Sulfur-Bridged Organodysprosium Single-Molecule Magnet. *Angew. Chem., Int. Ed.* **2012**, *51*, 6976.

(16) Berry, J. F. A Definitive Answer to a Bonding Quandary? The Role of One-Electron Resonance Structures in the Bonding of a $\{Cu_3S_2\}^{3+}$ Core. *Chem. - Eur. J.* **2010**, *16*, 2719.

(17) Berry, J. F. Two-Center/Three-Electron Sigma Half-Bonds in Main Group and Transition Metal Chemistry. *Acc. Chem. Res.* **2016**, *49*, 27.

(18) Yao, S. A.; Lancaster, K. M.; Götz, A. W.; DeBeer, S.; Berry, J. F. X-ray Absorption Spectroscopic, Crystallographic, Theoretical (DFT) and Chemical Evidence for a Chalcogen-Chalcogen Two-Center/Three-Electron Half Bond in an Unprecedented "Subselenide" $Se_2^{3-}$ Ligand. *Chem. - Eur. J.* **2012**, *18*, 9179.

(19) Yao, S. A.; Martin-Diaconescu, V.; Infante, I.; Lancaster, K. M.; Götz, A. W.; DeBeer, S.; Berry, J. F. Electronic Structure of $Ni_2E_2$ Complexes (E = S, Se, Te) and a Global Analysis of $M_2E_2$ Compounds: A Case for Quantized $E_2^{n-}$ Oxidation Levels with $n$ = 2, 3, or 4. *J. Am. Chem. Soc.* **2015**, *137*, 4993.

(20) (a) Arleth, N.; Bestgen, S.; Gamer, M. T.; Roesky, P. W. Realgar as a Building Block for Lanthanide Clusters: Encapsulation of a Copper Cluster by a Lanthanide Cluster. *J. Am. Chem. Soc.* **2014**, *136*, 14023. (b) Berg, D. J.; Andersen, R. A.; Zalkin, A. Electron-Transfer Chemistry of $(Me_5C_5)_2Yb$: Cleavage of Diorganoperoxide and Related Chalcogenides to give $(Me_5C_5)_2Yb(ER)(L)$ (E = O, S, Se, or Te; L = a Lewis Base). Crystal Structure of $(Me_5C_5)_2Yb$-$(TePh)(NH_3)$. *Organometallics* **1988**, *7*, 1858. (c) Berg, D. J.; Burns, C. J.; Andersen, R. A.; Zalkin, A. Electron-Transfer Reactions of Divalent Ytterbium Metallocenes. Synthesis of the Series $[(Me_5C_5)_2Yb]_2[\mu\text{-}E]$ (E = Oxygen, Sulfur, Selenium, or Tellurium) and Crystal Structure of $[(Me_5C5)_2Yb]_2[\mu\text{-}Se]$. *Organometallics* **1989**,

8, 1865. (d) Brewer, M.; Khasnis, D.; Buretea, M.; Berardini, M.; Emge, T. J.; Brennan, J. G. Pyridine Coordination Complexes of the Divalent Ytterbium Chalcogenolates Yb(EPh)$_2$ (E = S, Se, Te). *Inorg. Chem.* **1994**, *33*, 2743. (e) Kühling, M.; McDonald, R.; Liebing, P.; Hilfert, L.; Ferguson, M. J.; Takats, J.; Edelmann, F. T. Stabilization of Molecular Lanthanide Polysulfides by Bulky Scorpionate Ligands. *Dalton Trans.* **2016**, *45*, 10118. (f) Ma, Y. Z.; Pushkarevsky, N. A.; Sukhikh, T. S.; Galashov, A. E.; Makarov, A. G.; Roesky, P. W.; Konchenko, S. N. Steric Influence and Intermolecular Interactions of Formamidinate Ligands in Lanthanide (Sm, Yb) Arylchalcogenolate Complexes. *Eur. J. Inorg. Chem.* **2018**, *2018*, 3388. (g) Ma, Y.-Z.; Bestgen, S.; Gamer, M. T.; Konchenko, S. N.; Roesky, P. W. Polysulfide Coordination Clusters of the Lanthanides. *Angew. Chem., Int. Ed.* **2017**, *56*, 13249. (h) Recknagel, A.; Noltemeyer, M.; Stalke, D.; Pieper, U.; Schmidt, H.-G.; Edelmann, F. T. Monomere Organosamarium(III)chalkogenolate durch reduktive Spaltung von E-E-Bindungen (E = S, Se, Te). *J. Organomet. Chem.* **1991**, *411*, 347. (i) Zalkin, A.; Henly, T. J.; Andersen, R. A. Amminebis-(Pentamethylcyclopentadienyl)(Thiophenolato)Ytterbium(III). *Acta Crystallogr., Sect. C: Cryst. Struct. Commun.* **1987**, *43*, 233.

(21) Evans, W. J.; Miller, K. A.; Lee, D. S.; Ziller, J. W. Synthesis, Structure, and Ligand-Based Reduction Reactivity of Trivalent Organosamarium Benzene Chalcogenolate Complexes (C$_5$Me$_5$)$_2$Sm-(EPh)(THF) and [(C$_5$Me$_5$)$_2$Sm($\mu$-EPh)]$_2$. *Inorg. Chem.* **2005**, *44*, 4326.

(22) Hillier, A. C.; Liu, S.-Y.; Sella, A.; Elsegood, M. R. J. Lanthanide Chalcogenolate Complexes: Synthesis and Crystal Structures of the Isoleptic Series [Sm(Tp$^{Me,Me}$)$_2$ER] (E = O, S, Se, Te; Tp$^{Me,Me}$ = tris-3,5-dimethylpyrazolylborate). *Inorg. Chem.* **2000**, *39*, 2635.

(23) Werner, D.; Deacon, G. B.; Junk, P. C. Trapping CS$_2{}^{2-}$ and S$_3{}^{2-}$ between Two Ytterbium Formamidinates. *Inorg. Chem.* **2019**, *58*, 1912.

(24) Chilton, N. F.; Goodwin, C. A. P.; Mills, D. P.; Winpenny, R. E. P. The First Near-Linear Bis(amide) f-Block Complex: A Blueprint for a High Temperature Single Molecule Magnet. *Chem. Commun.* **2015**, *51*, 101.

(25) Goodwin, C. A. P.; Chilton, N. F.; Vettese, G. F.; Moreno Pineda, E.; Crowe, I. F.; Ziller, J. W.; Winpenny, R. E. P.; Evans, W. J.; Mills, D. P. Physicochemical Properties of Near-Linear Ln(II) Bis-Silylamide Complexes (Ln = Sm, Eu, Tm, Yb). *Inorg. Chem.* **2016**, *55*, 10057.

(26) Goodwin, C. A. P.; Réant, B. L. L.; Kragskow, J. G. C.; DiMucci, I. M.; Lancaster, K. M.; Mills, D. P.; Sproules, S. Heteroleptic Samarium(III) Halide Complexes Probed by Fluorescence-Detected L$_3$-Edge X-ray Absorption Spectroscopy. *Dalton Trans.* **2018**, *47*, 10613.

(27) (a) Evans, W. J.; Miller, K. A.; Ziller, J. W.; DiPasquale, A. G.; Heroux, K. J.; Rheingold, A. L. Formation of (C$_5$Me$_5$)$_2$U(EPh)Me, (C$_5$Me$_5$)$_2$U(EPh)$_2$, and (C$_5$Me$_5$)$_2$U($\eta^2$-TeC$_6$H$_4$) from (C$_5$Me$_5$)$_2$UMe$_2$ and PhEEPh (E = S, Se, Te). *Organometallics* **2007**, *26*, 4287. (b) Evans, W. J.; Takase, M. K.; Ziller, J. W.; DiPasquale, A. G.; Rheingold, A. L. Reductive Reactivity of the Tetravalent Uranium Complex [($\eta^5$-C$_5$Me$_5$)($\eta^8$-C$_8$H$_8$)U]$_2$($\mu$-$\eta^3$:$\eta^3$-C$_8$H$_8$). *Organometallics* **2009**, *28*, 236. (c) Gaunt, A. J.; Scott, B. L.; Neu, M. P. U(IV) Chalcogenolates Synthesized via Oxidation of Uranium Metal by Dichalcogenides. *Inorg. Chem.* **2006**, *45*, 7401. (d) Settineri, N. S.; Garner, M. E.; Arnold, J. A. Thorium Chalcogenolate Series Generated by Atom Insertion into Thorium–Carbon Bonds. *J. Am. Chem. Soc.* **2017**, *139*, 6261.

(28) Wu, W.; Rehe, D.; Hrobárik, P.; Kornienko, A. Y.; Emge, T. J.; Brennan, J. G. Molecular Thorium Compounds with Dichalcogenide Ligands: Synthesis, Structure, $^{77}$Se NMR Study, and Thermolysis. *Inorg. Chem.* **2018**, *57*, 14821.

(29) Matson, E. M.; Breshears, A. T.; Kiernicki, J. J.; Newell, B. S.; Fanwick, P. E.; Shores, M. P.; Walensky, J. R.; Bart, S. C. Trivalent Uranium Phenylchalcogenide Complexes: Exploring the Bonding and Reactivity with CS$_2$ in the Tp*$_2$UEPh Series (E = O, S, Se, Te). *Inorg. Chem.* **2014**, *53*, 12977.

(30) Nicholas, H. M.; Vonci, M.; Goodwin, C. A. P.; Loo, S. W.; Murphy, S. R.; Cassim, D.; Winpenny, R. E. P.; McInnes, E. J. L.; Chilton, N. F.; Mills, D. P. Electronic Structures of Bent Lanthanide-(III) Complexes with Two N-donor Ligands. *Chem. Sci.* **2019**, *10*, 10493.

(31) (a) Bochkarev, M. N.; Fagin, A. A. A New Route to Neodymium(II) and Dysprosium(II) Iodides. *Chem. - Eur. J.* **1999**, *5*, 2990. (b) Bochkarev, M. N.; Fedushkin, I. L.; Fagin, A. A.; Petrovskaya, T. V.; Ziller, J. W.; Broomhall-Dillard, R. N. R.; Evans, W. J. Synthesis and Structure of the First Molecular Thulium(II) Complex: [TmI$_2$(MeOCH$_2$CH$_2$OMe)$_3$]. *Angew. Chem., Int. Ed. Engl.* **1997**, *36*, 133. (c) Evans, W. J. Perspectives in Reductive Lanthanide Chemistry. *Coord. Chem. Rev.* **2000**, *206–207*, 263. (d) Evans, W. J.; Allen, N. T.; Workman, P. S.; Meyer, J. C. Large Scale Synthesis of Dysprosium and Neodymium Diiodides. *Inorg. Chem.* **2003**, *42*, 3097. (e) Evans, W. J.; Allen, N. T.; Ziller, J. W. The Availability of Dysprosium Diiodide as a Powerful Reducing Agent in Organic Synthesis: Reactivity Studies and Structural Analysis of DyI$_2$(DME)$_3$ and Its Naphthalene Reduction Product. *J. Am. Chem. Soc.* **2000**, *122*, 11749.

(32) (a) Brown, J. L.; Wu, G.; Hayton, T. W. Chalcogen Atom Transfer to Uranium(III): Synthesis and Characterization of [(R$_2$N)$_3$U]$_2$($\mu$-E) and [(R$_2$N)$_3$U]$_2$($\mu$-$\eta^2$:$\eta^2$-S$_2$) (R = SiMe$_3$; E = S, Se, Te). *Organometallics* **2013**, *32*, 1193. (b) Gardner, B. M.; King, D. M.; Tuna, F.; Wooles, A. J.; Chilton, N. F.; Liddle, S. T. Assessing Crystal Field and Magnetic Interactions in Diuranium-$\mu$-Chalcogenide Triamidoamine Complexes with U$^{IV}$–E–U$^{IV}$ Cores (E = S, Se, Te): Implications for Determining the Presence or Absence of Actinide–Actinide Magnetic Exchange. *Chem. Sci.* **2017**, *8*, 6207.

(33) Corbey, J. F.; Fang, M.; Ziller, J. W.; Evans, W. J. Cocrystallization of ($\mu$-S$_2$)$^{2-}$ and ($\mu$-S)$^{2-}$ and Formation of an [$\eta^2$-S$_3$N(SiMe$_3$)$_2$] Ligand from Chalcogen Reduction by (N$_2$)$^{2-}$ in a Bimetallic Yttrium Amide Complex. *Inorg. Chem.* **2015**, *54*, 801.

(34) Li, Y.; Pi, C.; Zhang, J.; Zhou, X.; Chen, Z.; Weng, L. Facile Transformations of Lanthanocene Alkyls to Lanthanocene Thiolate, Sulfide, and Disulfide Derivatives by Reaction with Elemental Sulfur. *Organometallics* **2005**, *24*, 1982.

(35) Evans, W. J.; Rabe, G. W.; Ziller, J. W.; Doedens, R. J. Utility of Organosamarium(II) Reagents in the Formation of Polyatomic Group 16 Element Anions: Synthesis and Structure of [(C$_5$Me$_5$)$_2$Sm]$_2$(E$_3$)-(THF), [(C$_5$Me$_5$)$_2$Sm(THF)]$_2$(E), and Related Species (E = S, Se, Te). *Inorg. Chem.* **1994**, *33*, 2719.

(36) (a) Avens, L. R.; Barnhart, D. M.; Burns, C. J.; McKee, S. D.; Smith, W. H. Oxidation Chemistry of a Uranium(III) Aryloxide. *Inorg. Chem.* **1994**, *33*, 4245. (b) Brennan, J. G.; Andersen, R. A.; Zalkin, A. Chemistry of Trivalent Uranium Metallocenes: Electron-Transfer Reactions. Synthesis and Characterization of [(Me-C$_5$H$_4$)$_3$U]$_2$E (E = S, Se, Te) and the Crystal Structures of Hexakis(methylcyclopentadienyl)sulfidodiuranium and Tris-(methylcyclopentadienyl)(triphenylphosphine oxide)uranium. *Inorg. Chem.* **1986**, *25*, 1761. (c) Camp, C.; Antunes, M. A.; García, G.; Ciofini, I.; Santos, I. C.; Pécaut, J.; Almeida, M.; Marçalo, J.; Mazzanti, M. Two-Electron versus One-Electron Reduction of Chalcogens by Uranium(III): Synthesis of a Terminal U(V) Persulfide Complex. *Chem. Sci.* **2014**, *5*, 841. (d) Fieser, M. E.; Johnson, C. W.; Bates, J. E.; Ziller, J. W.; Furche, F.; Evans, W. J. Dinitrogen Reduction, Sulfur Reduction, and Isoprene Polymerization via Photochemical Activation of Trivalent Bis(cyclopentadienyl) Rare-Earth-Metal Allyl Complexes. *Organometallics* **2015**, *34*, 4387. (e) Maria, L.; Soares, M.; Santos, I. C.; Sousa, V. R.; Mora, E.; Marçalo, J.; Luzyanin, K. V. A Novel Samarium(II) Complex Bearing a Dianionic Bis(phenolate) Cyclam Ligand: Synthesis, Structure and Electron-Transfer Reactions. *Dalton Trans.* **2016**, *45*, 3778.

(37) (a) Baccolini, G.; Boga, C.; Mazzacurati, M. Highly Atom-Economic One-Pot Formation of Three Different C-P Bonds: General Synthesis of Acyclic Tertiary Phosphine Sulfides. *J. Org. Chem.* **2005**, *70*, 4774. (b) Hayashi, M.; Matsuura, T.; Tanaka, I.; Ohta, H.; Watanabe, Y. Pd-Catalyzed P–C Cross-Coupling Reactions for Versatile Triarylphosphine Synthesis. *Org. Lett.* **2013**, *15*, 628.

(c) Kuhn, N.; Henkel, G.; Schumann, H.; Fröhlich, R. The Nature of the Bonding in Phosphane Tellurides. An Empirical NMR Study and the Crystal Structure of (iso-C$_3$H$_7$)$_3$PTe. *Z. Naturforsch., B: J. Chem. Sci.* **1990**, *45*, 1010. (d) Nordheider, A.; Woollins, J. D.; Chivers, T. Organophosphorus-Tellurium Chemistry: From Fundamentals to Applications. *Chem. Rev.* **2015**, *115*, 10378. (e) Zingaro, R. S.; Steeves, B. H.; Irgolic, K. Phosphine Tellurides. *J. Organomet. Chem.* **1965**, *4*, 320.

(38) Sur, S. K. Measurement of Magnetic Susceptibility and Magnetic Moment of Paramagnetic Molecules in Solution by High-Field Fourier Transform NMR Spectroscopy. *J. Magn. Reson.* **1989**, *82*, 169.

(39) Sorace, L.; Gatteschi, D. Electronic Structure and Magnetic Properties of Lanthanide Molecular Complexes. In *Lanthanides and Actinides in Molecular Magnetism*; Layfield, R. A., Murugesu, M., Eds.; Wiley-VCH: Weinheim, Germany, 2015; pp 1−26.

(40) van Vleck, J. H. *Theory of Electric and Magnetic Susceptibilities*; Oxford University Press: Oxford, UK, 1932.

(41) Chivers, T.; Laitinen, R. S. Tellurium: A Maverick among the Chalcogens. *Chem. Soc. Rev.* **2015**, *44*, 1725. (b) Mulliken, R. S. The Nature of the Chemical Bond. By Linus Pauling. *J. Phys. Chem.* **1940**, *44*, 827.

(42) Goodwin, C. A. P.; Chilton, N. F.; Natrajan, L. S.; Boulon, M.-E.; Ziller, J. W.; Evans, W. J.; Mills, D. P. An Investigation into the Effects of a Trigonal Planar Ligand Field on the Electronic Properties of Lanthanide(II) Tris(silylamide) Complexes (Ln = Sm, Eu, Tm, Yb). *Inorg. Chem.* **2017**, *56*, 5959.

(43) Goodwin, C. A. P.; Joslin, K. C.; Lockyer, S. J.; Formanuik, A.; Morris, G. A.; Ortu, F.; Vitorica-Yrezabal, I. J.; Mills, D. P. Homoleptic Trigonal Planar Lanthanide Complexes Stabilized by Superbulky Silylamide Ligands. *Organometallics* **2015**, *34*, 2314.

(44) (a) Goodwin, C. A. P.; Tuna, F.; McInnes, E. J. L.; Liddle, S. T.; McMaster, J.; Vitorica-Yrezabal, I. J.; Mills, D. P. [U$^{III}${N-(SiMe$_2$tBu)$_2$}$_3$]: A Structurally Authenticated Trigonal Planar Actinide Complex. *Chem. - Eur. J.* **2014**, *20*, 14579. (b) Goodwin, C. A. P.; Tuna, F.; McInnes, E. J. L.; Mills, D. P. Exploring Synthetic Routes to Heteroleptic U$^{III}$, U$^{IV}$, and Th$^{IV}$ Bulky Bis(silyl)amide Complexes. *Eur. J. Inorg. Chem.* **2018**, *2018*, 2356.

(45) Li, J.; Hao, J.; Cui, C. Reactivity of Ytterbium(II) Silylamide Supported by a Pyrrolyl−Cyclopentadienyl Ligand. *Dalton Trans.* **2015**, *44*, 767.

(46) Melman, J. H.; Fitzgerald, M.; Freedman, D.; Emge, T. J.; Brennan, J. G. Chalcogen-Rich Lanthanide Clusters from Lanthanide Halide Starting Materials: A New Approach to the Low-Temperature Synthesis of LnS$_x$ Solids from Molecular Precursors. *J. Am. Chem. Soc.* **1999**, *121*, 10247.

(47) (a) Zhang, Z.; Zhang, L.; Li, Y.; Hong, L.; Chen, Z.; Zhou, X. Activation of Bis(guanidinate)lanthanide Alkyl and Aryl Complexes on Elemental Sulfur: Synthesis and Characterization of Bis-(guanidinate)lanthanide Thiolates and Disulfides. *Inorg. Chem.* **2010**, *49*, 5715. (b) Gu, D.; Yi, C.; Ren, W. Lanthanocene and Cerocene Alkyl Complexes: Synthesis, Structure, and Reactivity Studies. *Inorg. Chem.* **2019**, *58*, 9260.

(48) Fagin, A. A.; Fukin, G. K.; Cherkasov, A. V.; Shestakov, A. F.; Pushkarev, A. P.; Balashova, T. V.; Maleev, A. A.; Bochkarev, M. N. Ln$_3$I$_5$(S$_2$N$_2$)(S$_2$)(THF)$_{10}$ − A New Type of Molecular Compounds. *Dalton Trans.* **2016**, *45*, 4558.

(49) Shannon, R. D. Revised Effective Ionic Radii and Systematic Studies of Interatomic Distances in Halides and Chalcogenides. *Acta Crystallogr., Sect. A: Cryst. Phys., Diffr., Theor. Gen. Crystallogr.* **1976**, *32*, 751.

(50) Evans, W. J.; Nyce, G. W.; Clark, R. D.; Doedens, R. J.; Ziller, J. W. The Trivalent Neodymium Complex [(C$_5$Me$_5$)$_3$Nd] Is a One-Electron Reductant! *Angew. Chem., Int. Ed.* **1999**, *38*, 1801.

(51) Evans, W. J.; Gonzales, S. L.; Ziller, J. W. X-ray Crystal Structure of the First Dibismuth Complex Containing a Planar M$_2$($\mu$-$\eta^2$:$\eta^2$-Bi$_2$) Unit. *J. Am. Chem. Soc.* **1991**, *113*, 9880.

(52) (a) Bünzli, J.-C. G.; Eliseeva, S. V. In *Lanthanide Luminescence*; Hännninen, P., Härmä, H., Eds.; Springer-Verlag: Berlin, 2011; p 1.

(b) Dieke, G. H.; Crosswhite, H. M. The Spectra of the Doubly and Triply Ionized Rare Earths. *Appl. Opt.* **1963**, *2*, 675. (c) van der Ende, B. M.; Aarts, L.; Meijerink, A. Lanthanide Ions as Spectral Converters for Solar Cells. *Phys. Chem. Chem. Phys.* **2009**, *11*, 11081.

(53) Jayarathne, U.; Chandrasekaran, P.; Greene, A. F.; Mague, J. T.; DeBeer, S.; Lancaster, K. M.; Sproules, S.; Donahue, J. P. X-ray Absorption Spectroscopy Systematics at the Tungsten L-Edge. *Inorg. Chem.* **2014**, *53*, 8230.

(54) Brouder, C. Angular Dependence of X-ray Absorption Spectra. *J. Phys.: Condens. Matter* **1990**, *2*, 701.

(55) MacMillan, S. N.; Lancaster, K. M. X-ray Spectroscopic Interrogation of Transition-Metal-Mediated Homogeneous Catalysis: Primer and Case Studies. *ACS Catal.* **2017**, *7*, 1776.

(56) (a) Hämäläinen, K.; Siddons, D. P.; Hastings, J. B.; Berman, L. E. Elimination of the Inner-Shell Lifetime Broadening in X-ray-Absorption Spectroscopy. *Phys. Rev. Lett.* **1991**, *67*, 2850. (b) Kvashnina, K. O.; Butorin, S. M.; Glatzel, P. Direct Study of the f-Electron Configuration in Lanthanide Systems. *J. Anal. At. Spectrom.* **2011**, *26*, 1265.

(57) Fieser, M. E.; Ferrier, M. G.; Su, J.; Batista, E. R.; Cary, S. K.; Engle, J. W.; Evans, W. J.; Lezama Pacheco, J. S.; Kozimor, S. A.; Olson, A. C.; Ryan, A. J.; Stein, B. W.; Wagner, G. L.; Woen, D. H.; Vitova, T.; Yang, P. Evaluating the Electronic Structure of Formal Ln$^{II}$ Ions in Ln$^{II}$(C$_5$H$_4$SiMe$_3$)$_3$$^{1−}$ using XANES Spectroscopy and DFT Calculations. *Chem. Sci.* **2017**, *8*, 6076.

(58) (a) Banerjee, P.; Sproules, S.; Weyhermüller, T.; DeBeer George, S.; Wieghardt, K. Electronic Structure of the [Tris-(dithiolene)chromium]$^z$ (z = 0, 1−, 2−, 3−) Electron Transfer Series and Their Manganese(IV) Analogues. An X-ray Absorption Spectroscopic and Density Functional Theoretical Study. *Inorg. Chem.* **2009**, *48*, 5829. (b) Corcos, A. R.; Villanueva, O.; Walroth, R. C.; Sharma, S. K.; Bacsa, J.; Lancaster, K. M.; MacBeth, C. E.; Berry, J. F. Oxygen Activation by Co(II) and a Redox Non-Innocent Ligand: Spectroscopic Characterization of a Radical−Co(II)−Superoxide Complex with Divergent Catalytic Reactivity. *J. Am. Chem. Soc.* **2016**, *138*, 1796. (c) Milsmann, C.; Sproules, S.; Bill, E.; Weyhermüller, T.; DeBeer George, S.; Wieghardt, K. Stabilization of High-Valent Fe$^{IV}$S$_6$-Cores by Dithiocarbamate(1−) and 1,2-Dithiolate(2−) Ligands in Octahedral [Fe$^{IV}$(Et$_2$dtc)$_{3−n}$(mnt)$_n$]$^{(n−1)−}$ Complexes (n = 0, 1, 2, 3): A Spectroscopic and Density Functional Theory Computational Study. *Chem. - Eur. J.* **2010**, *16*, 3628. (d) Morsing, T. J.; MacMillan, S. N.; Uebler, J. W. H.; Brock-Nannestad, T.; Bendix, J.; Lancaster, K. M. Stabilizing Coordinated Radicals via Metal-Ligand Covalency: A Structural, Spectroscopic, and Theoretical Investigation of Group 9 Tris(dithiolene) Complexes. *Inorg. Chem.* **2015**, *54*, 3660. (e) Sproules, S.; Benedito, F. L.; Bill, E.; Weyhermüller, T.; DeBeer George, S.; Wieghardt, K. Characterization and Electronic Structures of Five Members of the Electron Transfer Series [Re(benzene-1,2-dithiolato)$_3$]$^z$ (z = 1+, 0, 1−, 2−, 3−). A Spectroscopic and Density Functional Theoretical Study. *Inorg. Chem.* **2009**, *48*, 10926. (f) Sproules, S.; Wieghardt, K. Dithiolene radicals: Sulfur K-edge X-ray Absorption Spectroscopy and Harry's Intuition. *Coord. Chem. Rev.* **2011**, *255*, 837. (g) Varela-Álvarez, A.; Yang, T.; Jennings, H.; Kornecki, K. P.; MacMillan, S. N.; Lancaster, K. M.; Mack, J. B. C.; Du Bois, J.; Berry, J. F.; Musaev, D. G. Rh$_2$(II,III) Catalysts with Chelating Carboxylate and Carboxamidate Supports: Electronic Structure and Nitrene Transfer Reactivity. *J. Am. Chem. Soc.* **2016**, *138*, 2327. (h) Walroth, R. C.; Lukens, J. T.; MacMillan, S. N.; Finkelstein, K. D.; Lancaster, K. M. Spectroscopic Evidence for a 3d$^{10}$ Ground State Electronic Configuration and Ligand Field Inversion in [Cu(CF$_3$)$_4$]$^{1-}$. *J. Am. Chem. Soc.* **2016**, *138*, 1922. (i) Walroth, R. C.; Uebler, J. W. H.; Lancaster, K. M. Probing Cu$^I$ in Homogeneous Catalysis using High-Energy-Resolution Fluorescence-Detected X-ray Absorption Spectroscopy. *Chem. Commun.* **2015**, *51*, 9864. (j) Wilding, M. J. T.; Iovan, D. A.; Wrobel, A. T.; Lukens, J. T.; MacMillan, S. N.; Lancaster, K. M.; Betley, T. A. Direct Comparison of C−H Bond Amination Efficacy through Manipulation of Nitrogen-Valence Centered Redox: Imido versus Iminyl. *J. Am. Chem. Soc.* **2017**, *139*, 14757.

(59) (a) Fieser, M. E.; MacDonald, M. R.; Krull, B. T.; Bates, J. E.; Ziller, J. W.; Furche, F.; Evans, W. J. Structural, Spectroscopic, and Theoretical Comparison of Traditional vs Recently Discovered $Ln^{2+}$ Ions in $[K(2.2.2\text{-}cryptand)][(C_5H_4SiMe_3)_3Ln]$ Complexes: The Variable Nature of $Dy^{2+}$ and $Nd^{2+}$. *J. Am. Chem. Soc.* **2015**, *137*, 369. (b) MacDonald, M. R.; Bates, J. E.; Fieser, M. E.; Ziller, J. W.; Furche, F.; Evans, W. J. Expanding Rare-Earth Oxidation State Chemistry to Molecular Complexes of Holmium(II) and Erbium(II). *J. Am. Chem. Soc.* **2012**, *134*, 8420. (c) MacDonald, M. R.; Bates, J. E.; Ziller, J. W.; Furche, F.; Evans, W. J. Completing the Series of + 2 Ions for the Lanthanide Elements: Synthesis of Molecular Complexes of $Pr^{2+}$, $Gd^{2+}$, $Tb^{2+}$, and $Lu^{2+}$. *J. Am. Chem. Soc.* **2013**, *135*, 9857. (d) Meihaus, K. R.; Fieser, M. E.; Corbey, J. F.; Evans, W. J.; Long, J. R. Record High Single-Ion Magnetic Moments Through $4f^n5d^1$ Electron Configurations in the Divalent Lanthanide Complexes $[(C_5H_4SiMe_3)_3Ln]^-$. *J. Am. Chem. Soc.* **2015**, *137*, 9855.

(60) (a) Perdew, J. P.; Burke, K.; Ernzerhof, M. Generalized Gradient Approximation Made Simple (PBE0). *Phys. Rev. Lett.* **1996**, *77*, 3865. (b) Perdew, J. P.; Burke, K.; Ernzerhof, M. Erratum: Generalized Gradient Approximation Made Simple. *Phys. Rev. Lett.* **1997**, *78*, 1396.

(61) Chai, J.-D.; Head-Gordon, M. Systematic Optimization of Long-Range Corrected Hybrid Density Functionals. *J. Chem. Phys.* **2008**, *128*, No. 084106.

(62) (a) Adamo, C.; Barone, V. Toward Reliable Density Functional Methods without Adjustable Parameters: The PBE0Model. *J. Chem. Phys.* **1999**, *110*, 6158. (b) Ernzerhof, M.; Scuseria, G. E. Assessment of the Perdew-Burke-Ernzerhof Exchange-Correlation Functional. *J. Chem. Phys.* **1999**, *110*, 5029.

(63) (a) Becke, A. D. Density-Functional Thermochemistry. III. The Role of Exact Exchange. *J. Chem. Phys.* **1993**, *98*, 5648. (b) Becke, A. D. A New Mixing of Hartree-Fock and Local Density-Functional Theories. *J. Chem. Phys.* **1993**, *98*, 1372.

(64) Zhao, Y.; Truhlar, D. G. The M06 Suite of Density Functionals for Main Group Thermochemistry, Thermochemical Kinetics, Noncovalent Interactions, Excited States, and Transition Elements: Two New Functionals and Systematic Testing of Four M06-Class Functionals and 12 Other Functionals. *Theor. Chem. Acc.* **2008**, *120*, 215.

(65) Pantazis, D. A.; Neese, F. All-Electron Scalar Relativistic Basis Sets for the Lanthanides. *J. Chem. Theory Comput.* **2009**, *5*, 2229.

(66) (a) Fitzgerald, M.; Emge, T. J.; Brennan, J. G. Chalcogen-Rich Lanthanide Clusters with Fluorinated Thiolate Ligands. *Inorg. Chem.* **2002**, *41*, 3528. (b) Huebner, L.; Kornienko, A.; Emge, T. J.; Brennan, J. G. Lanthanide Clusters with Internal Ln: Fragmentation and the Formation of Dimers with Bridging $Se^{2-}$ and $Se_2^{2-}$ Ligands. *Inorg. Chem.* **2005**, *44*, 5118. (c) Stuber, M. A.; Kornienko, A. Y.; Emge, T. J.; Brennan, J. G. Tetrametallic Thorium Compounds with $Th_4E_4$ (E = S, Se) Cubane Cores. *Inorg. Chem.* **2017**, *56*, 10247.

(67) Rajeshkumar, T.; Rajaraman, G. Is a Radical Bridge a Route to Strong Exchange Interactions in Lanthanide Complexes? A Computational Examination. *Chem. Commun.* **2012**, *48*, 7856.

(68) Zhang, Y.-Q.; Luo, C.-L.; Wang, B.-W.; Gao, S. Understanding the Magnetic Anisotropy in a Family of $N_2^{3-}$ Radical-Bridged Lanthanide Complexes: Density Functional Theory and ab Initio Calculations. *J. Phys. Chem. A* **2013**, *117*, 10873.

(69) (a) Ruiz, E.; Alvarez, S.; Cano, J.; Polo, V. About the Calculation of Exchange Coupling Constants using Density-Functional Theory: The Role of the Self-Interaction Error. *J. Chem. Phys.* **2005**, *123*, 164110. (b) Ruiz, E.; Cano, J.; Alvarez, S.; Alemany, P. Broken Symmetry Approach to Calculation of Exchange Coupling Constants for Homobinuclear and Heterobinuclear Transition Metal Complexes. *J. Comput. Chem.* **1999**, *20*, 1391.

(70) Hey, E.; Lappert, M. F.; Atwood, J. L.; Bott, S. G. Bis(trimethylsilyl)phosphinodithioformates, the Phosphorus Analogues of Dithiocarbamates; X-ray Structure of $[Zr(cp)_2(Cl)(\eta^2\text{-}S_2CPR_2)]$ and Its Thermolysis Product $[\{Zr(cp)_2(\mu\text{-}S)\}_2]$(cp = $\eta$-$C_5H_5$, R = $SiMe_3$). *J. Chem. Soc., Chem. Commun.* **1987**, 421.

(71) (a) Gaunt, A. J.; Reilly, S. D.; Enriquez, A. E.; Scott, B. L.; Ibers, J. A.; Sekar, P.; Ingram, K. I.; Kaltsoyannis, N.; Neu, M. P. Experimental and Theoretical Comparison of Actinide and Lanthanide Bonding in $M[N(ER_2)_2]_3$ Complexes (M = U, Pu, La, Ce; E = S, Se, Te; R = Ph, *i*Pr, H). *Inorg. Chem.* **2008**, *47*, 29. (b) Krogh-Jespersen, K.; Romanelli, M. D.; Melman, J. H.; Emge, T. J.; Brennan, J. G. Covalent Bonding and the Trans Influence in Lanthanide Compounds. *Inorg. Chem.* **2010**, *49*, 552.

(72) Alvarez, S. A Cartography of the van der Waals Territories. *Dalton Trans.* **2013**, *42*, 8617.

(73) Yao, S.; Xiong, Y.; Zhang, X.; Schlangen, M.; Schwarz, H.; Milsmann, C.; Driess, M. Facile Dissociation of $[(LNi^{II})_2E_2]$ Dichalcogenides: Evidence for $[LNi^{II}E_2]$ Superselenides and Supertellurides in Solution. *Angew. Chem., Int. Ed.* **2009**, *48*, 4551.

(74) (a) Leng, J.-D.; Goodwin, C. A. P.; Vitorica-Yrezabal, I. J.; Mills, D. P. Salt Metathesis Routes to Homoleptic Near-Linear Mg(II) and Ca(II) Bulky Bis(silyl)amide Complexes. *Dalton Trans.* **2018**, *47*, 12526. (b) Nicholas, H. M.; Goodwin, C. A. P.; Kragskow, J. G. C.; Lockyer, S. J.; Mills, D. P. Structural Characterization of Lithium and Sodium Bulky Bis(silyl)amide Complexes. *Molecules* **2018**, *23*, 1138.